Theoretical and Applied Fracture Mechanics 118 (2022) 103260

Contents lists available at ScienceDirect

Theoretical and Applied Fracture Mechanics

journal homepage: www.elsevier.com/locate/tafmec

3D contact effects in fretting fatigue tests

J. Vázquez, D. Erena *, C. Navarro, J. Domínguez

Departamento de Ingeniería Mecánica y Fabricación, Universidad de Sevilla, Camino de los Descubrimientos s/n, C.P 41092, Sevilla, Spain

ARTICLE INFO

Keywords:
Fretting fatigue
Cylindrical contact
3D geometrical effects
FEM

ABSTRACT

Fretting fatigue is a material damage phenomenon produced in mechanical contacts. This phenomenon mainly produces surface cracking, and depending on the fretting regime, surface wear. In the bibliography many different types of fretting tests, with different geometries have been proposed. This paper numerically analyses, via FEM models, some fretting tests with cylindrical pads and test specimens having different geometries that are frequently used in the literature. In such cases, non-negligible 3D effects are produced. The differences between the contact stress field obtained with different approaches are analysed and discussed.

1. Introduction

Fretting fatigue is a material damage phenomenon produced when two mechanical elements, that are pressed together, are subjected to time variable bulk loads, generally cyclic. The mismatch of the strains produced between both contacting surfaces leads to a relative displacement (slip) between them, at least partially. This relative displacement, in junction with the friction, produce tangential tractions on the surface which generate high stresses and strains close to the contacting surfaces [1]. The time-varying nature of these stresses and strains fields produces fatigue crack initiation and crack growth. The crack growth rate of these cracks depends on the bulk loads applied to the components, materials and many other parameters [2]. If cracks stop growing away from the surface or rotate to grow towards the surface, producing some kind of pitting, the phenomenon is called fretting wear. If the bulk stresses make the crack to continue growing from the surface until the final fracture of the component, the phenomenon is called fretting fatigue.

Fretting fatigue is produced in many different systems. There are many examples of fretting fatigue failures in mechanical joints, such as rotor-blade connections in gas or vapour turbines, or in bolted, riveted and in shaft-hub connections [3]. It can also be produced in cables for electric conduction or structural applications [3].

Fretting fatigue depends on different factors, some common to the majority of fatigue processes and others typical of fretting. These include the contact pressure between the elements, the friction coefficient, tangential forces on surfaces, surfaces roughness or the amplitude of relative slip between them. In addition, the stress state near the initiation point has a high gradient, is strongly multiaxial and their components vary out of phase. An idea of the complexity of the phenomenon and the effect of some parameters can be found in the literature [2,4–7].

To analyse and understand the fretting fatigue phenomenon, many different types of tests have been proposed [8,9]. The types of tests can be divided into two groups: those trying to reproduce real situations, considering real geometries and loads, and other group of tests with simple loads and contacting geometries. In these last type of tests, the surfaces of the contacting bodies are usually spherical, cylindrical, plane and plane with rounded edges. The first group is used normally to check the capability of a real system to support the expected loads during the required working time and also to improve the fretting fatigue strength of actual designs. The complexity of the contact conditions and geometries in those cases makes very difficult to relate the failure process to the local stress and strain conditions close to the crack initiation points. That is the reason why, to better understand the phenomenon and to analyse the effect of different parameters on the fretting fatigue strength and life, tests with simple geometries and loads are carried out for research. In these tests, by using simple contact geometries, it is possible to know more precisely the stress and strain fields produced close to the contact zone, where cracks initiate and so to relate these fields with the crack initiation and propagation lives. These last types of tests are standardised [8,9] and have been carried out by many researchers [4,10–17].

Although there have been some research groups doing tests with spherical contact [4,16–19] which is the simplest and easiest type of test, chiefly due to assembly and alignment issues, most researchers made tests with cylindrical, plane or plane with rounded edges [20,21], which are closer to real contact conditions, but simpler. In these three cases, most researchers relate the crack initiation and growth process with the stresses and strains fields by using analytical or numerical 2D

* Corresponding author.
E-mail address: deg@us.es (D. Erena).

https://doi.org/10.1016/j.tafmec.2022.103260
Received 15 October 2021; Received in revised form 14 January 2022; Accepted 16 January 2022
Available online 8 February 2022

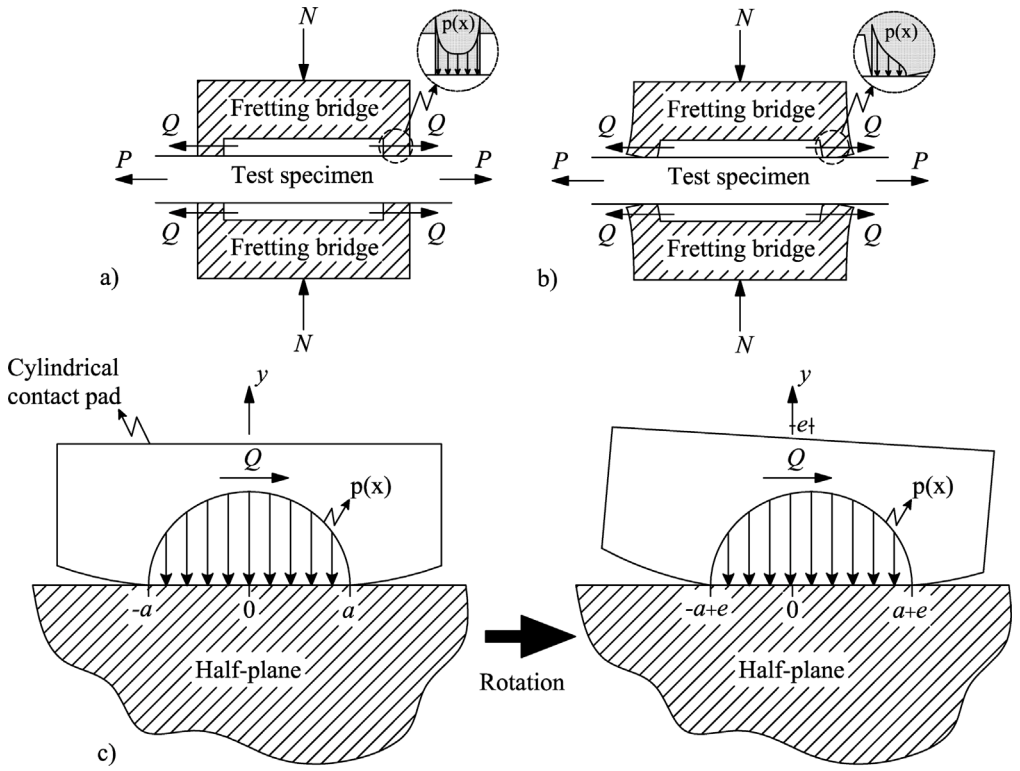

Fig. 1. (a) Scheme of an ideal fretting bridge, (b) Rotation due to tangential loading in the pads of the fretting bridge. (b) Rotation in a cylindrical pad.

solutions, in most cases assuming plane strain behaviour, in order to reproduce these fields. Mutoh et al. [22], used pads with a flat surface mounted in fretting bridges to analyse the fretting fatigue process, and related the crack initiation and propagation with the stresses obtained with a 2D model [23,24]. Similar analyses have been made by other researchers [25,26]. Hills and Nowell, and their group [10,11,13,27], as well as Szolwinski and Farris [12] and other researchers [14,15,28–30] carried out many fretting fatigue tests with cylindrical contact. They used mainly a 2D analytical solution [31] to relate stresses and fretting fatigue process.

Approaching an actual contact pair, under normal and tangential loads, by means of a 2D model is a simple and accurate approach, but some cautions should be taken in the experimental procedure in order to be sure that the conditions to apply the analytical or numerical 2D approach are given. Otherwise, the theoretical or numerical 2D stress/strain solution may not reproduce the actual stress states. One important aspect in the experimental setup is that, as far as possible, the rotations of the pads must be avoided, because this issue would change the stress distributions and the position of the contact zone. Fig. 1a depicts schematically a fretting bridge with flat pads and the theoretical symmetric stress distribution usually assumed for 2D calculations (Fig. 1a). On the other hand, Fig. 1b shows a possible stress distribution in case of rotation of the pad produced by the tangential contact loads in a flexible bridge. In such situation, the stress distribution will be quite different to the symmetrical one (no rotation) and therefore the results obtained with the model without considering the possible rotation may not be useful. In case of cylindrical contact, and assuming that the normal and tangential forces do not change with the rotation of the contact pad, there is no variation of the stress distribution in the contact zone, but the rotation of the pad will produce rolling of it and a motion of the contact zone, and thus modifying the contact zone location in the specimen (Fig. 1c). Usually, the stiffness of the fretting bridges used for testing is high enough to guarantee that the rotation is small, and thus producing small stress variations relative to the theoretical ones. Anyway, an analysis before testing to check that the rotations in a certain fretting bridge are small enough, should be carried out.

In order to properly model a contact pair using a two-dimensional model, it is important to analyse and compare the contact stress distributions produced by 2D and 3D models. The authors' previous work [32], showed that a non-negligible difference in fretting fatigue life predictions are obtained between 2D and 3D approaches. This paper analyses several fretting tests with cylindrical pads and test specimens having typical geometries used in the literature. In such cases, 3D effects are produced which are not considered when a 2D approach is used. To understand these effects, 3D finite element models (FEM) are carried out over several geometries used by different authors and then compared with the frequently assumed 2D approach used in order to analyse the effect of different stress/strain parameters on the fretting fatigue behaviour. The differences between different approaches are analysed and discussed.

2. Fretting fatigue tests configurations

From the beginning of testing with fretting bridges different pad-specimen geometries have been used. Mutoh et al. [33] used a flat pad with a contact width usually longer than the specimen width (Fig. 2a) and a specimen having a cross section that was not rectangular. Nowell, Hills et al. [11] made many of their tests with cylindrical contact and a pad-specimen geometry as represented schematically in Fig. 2b. Szolwinski and Farris [12], used cylindrical pads with the same width as the test specimens, Fig. 2c. Mall et al. [6] as well as Noraphaiphipaksa et al. [34] used cylindrical pads whose thickness was longer than that of test specimens (Fig. 2d). In tests configurations shown in Fig. 2a and 2d, the width of contact zone is smaller than that of contact pad and thus leading to a notable stress raiser in the borders of the contact zone. Table 1 shows the summary of a review made about the different types of geometries and analysis used for fretting fatigue test in the bibliography. Schemes for the pads and test specimens geometries used in these tests are shown in Fig. 2f1 to f7.

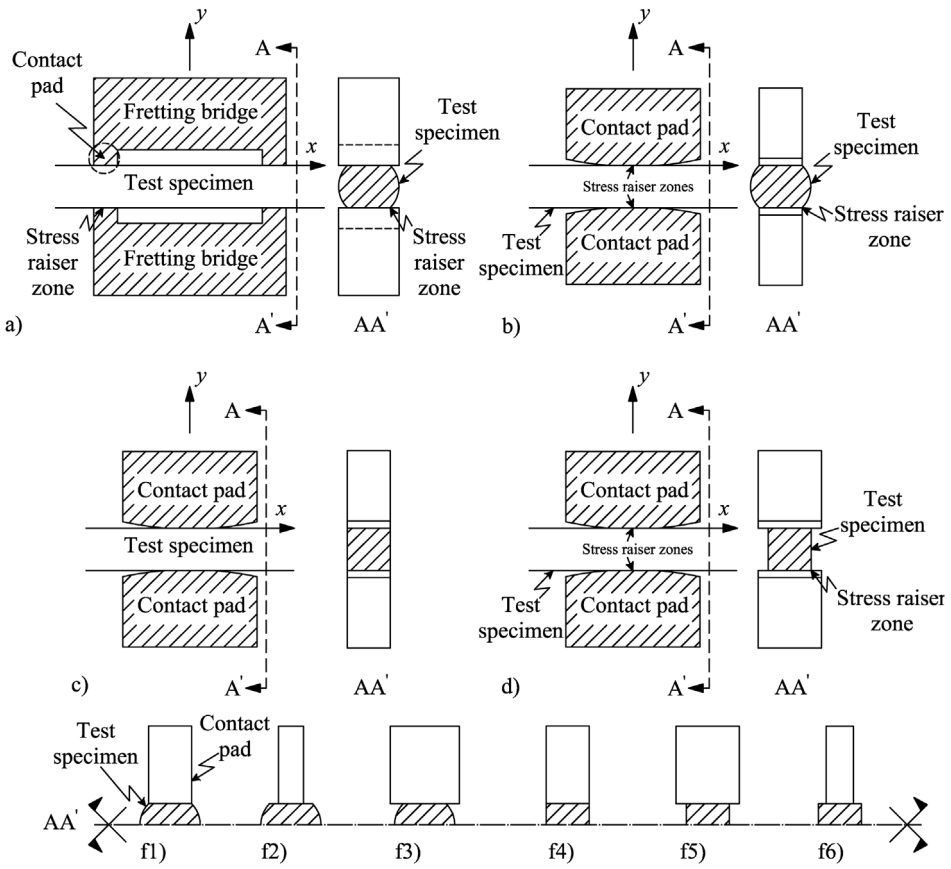

Fig. 2. Different test configurations frequently used in the bibliography.

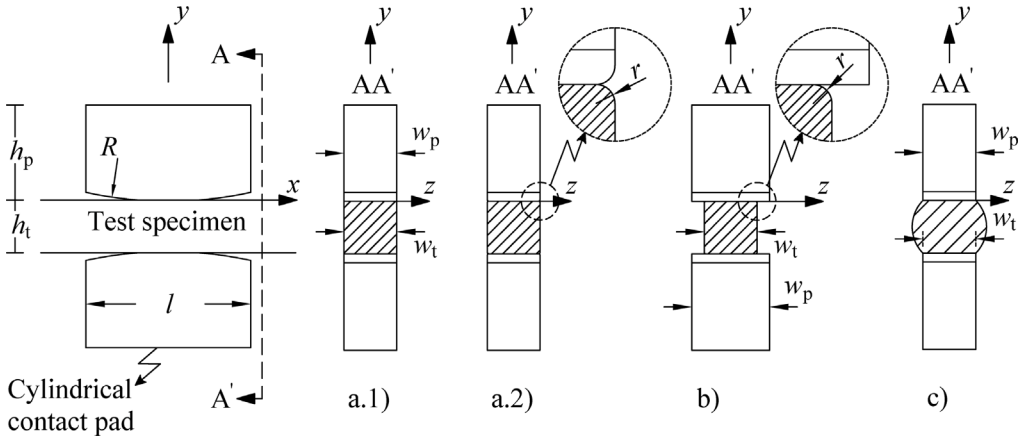

Fig. 3. Test configurations analysed.

The ASTM Standard E2789 [8] gives some recommendations for fretting fatigue testing, but does not include any recommendation about the pad-specimen geometries to be used. But, depending on the geometry considered, 3D effects make the stress distribution produced along the contact width to be different, so that test results may not be comparable between different configurations. Also those 3D stresses are different to that obtained with a 2D numerical or analytical solution. For instance, in the case of cylindrical contact, for the same pad radius and the same loads applied, the stress distributions produced in the specimen are different in the three cases represented in Fig. 2b to 2d. So the test results obtained with these geometries are not directly comparable if a 2D model is used in all cases to analyse the stress and strain fields.

3. Cases analysed

The cases analysed in the present paper are shown in Fig. 3a to c, which correspond to the most usual test configurations found in the bibliography. These configurations can be grouped into two general cases: a first case (Figs. 3a.1, 3a.2 and 3c) in which the fretting fatigue test specimen and contact pad have the same width at the contact zone, and a second case in which at the contact zone the test specimen's width is shorter than contact pad's width, i.e., $w_t < w_p$ (Fig. 3b). A fillet is included in cases shown in Figs. 3a.2 and 3b; in the former it is included to analyse a geometry that resembles that obtained after a typical machining process (a sharp edge is not a real feature), whereas in the latter, and in addition to consider a real (machined) corner, the

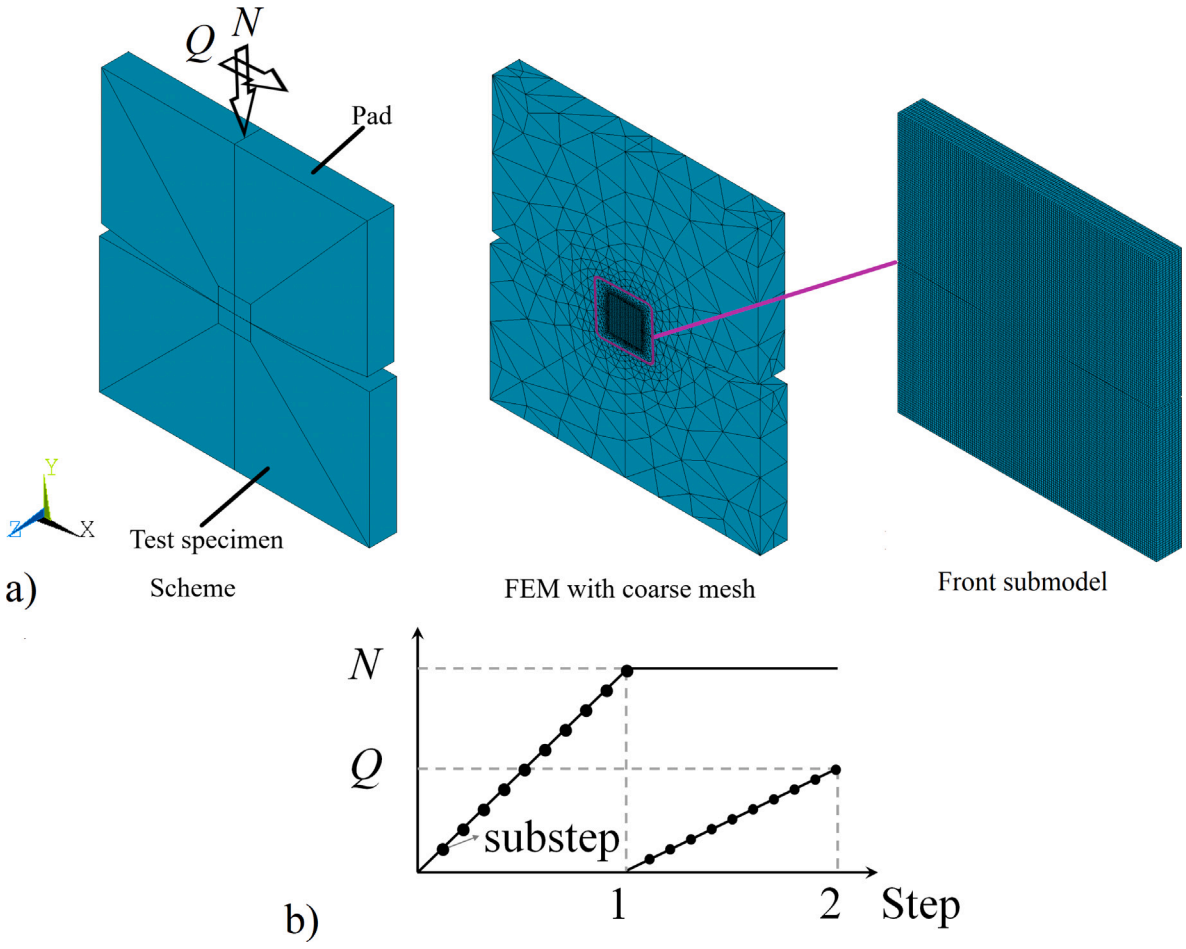

Fig. 4. (a) Details of FEM model used, (b) Fretting loads application in the model.

Table 1
A compilation of different tests configurations used in the bibliography.

Ref.	Geom.[a]	Cont. Pad[b]	Type anal.[c]	Ref.	Geom.[a]	Cont. Pad[b]	Type anal.[c]
[35]	f1	Flat	Num. & Exp.	[36]	f1	Cyl.	Anal. & Exp.
[24]	f1	Flat	Num.	[37]	Unspec.	Cyl.	Num. & Exp.
[38]	f1	Flat	Num. & Exp.	[39]	f5	Cyl. & Flat	Anal. & Exp.
[40]	f1	Flat	Num. & Exp.	[41]	f5	Cyl. & Flat	Num. & Exp.
[42]	f6	Flat	Exp.	[43]	f5	F.R.	Num. & Exp.
[44]	f5	Cyl.	Num.	[45]	f5	F.R.	Num. & Exp.
[46]	f5	Cyl.	Num.	[47]	f5	F.R.	Num.
[48]	f5	Cyl.	Num. & Exp.	[49]	f5	F.R.	Num.
[50]	Unspec.	Cyl.	Anal. & Exp.	[20]	f5	F.R.	Exp.
[51]	f4	Cyl.	Num. & Exp.	[14]	f4	Cyl.	Num. & Exp.
[52]	f4	Cyl.	Num. & Exp.	[26]	f4	Cyl.	Exp.
[53]	Unspec.	Cyl. & F.R.	Num. & Exp.	[54]	f5	Cyl.	Exp.
[55]	Unspec.	Cyl. & F.R.	Num. & Exp.	[56]	f5	Cyl.	Num. & Exp.
[57]	f4	Cyl.	Anal. & Exp.	[58]	f5	Cyl.	Exp.
[59]	f4	Cyl.	Exp.	[60]	f4	Flat	Num. & Exp.
[12]	f4	Cyl.	Anal. & Exp.	[61]	f5	Cyl.	Num. & Exp.
[62]	f4	Cyl.	Num. & Exp.	[63]	f3	Cyl. & Flat	Anal. & Exp.
[64]	f5	Flat	Num. & Exp.	[65]	f5	Flat	Exp.
[66]	f5	Flat	Num. & Exp.	[21]	f5	Flat	Exp.
[67]	f5	Flat	Num. & Exp.	[38]	f2	Flat	Num. & Exp.
[68]	f5	Flat	Exp.	[69]	f3	Flat	Exp.
[70]	f1	Cyl.	Anal. & Exp.	[71]	f5	Flat	Exp.
[72]	f4	Cyl.	Anal. & Exp.	[73]	f5	Flat	Exp.
[74]	f4	Cyl.	Anal. & Exp.	[75]	f3	Flat	Exp.
[27]	f5	Cyl.	Anal., Num. & Exp				

[a]See Figure 2f1 to 2f6 for an explanation (Unspec.=unspecified).
[b]Type of contact pad: Cyl.=cylindrical, F.R.=Flat with rounded ends.
[c]Type of analysis of the contact: Exp.=experimental, Anal.=analytic, Num.=numeric.

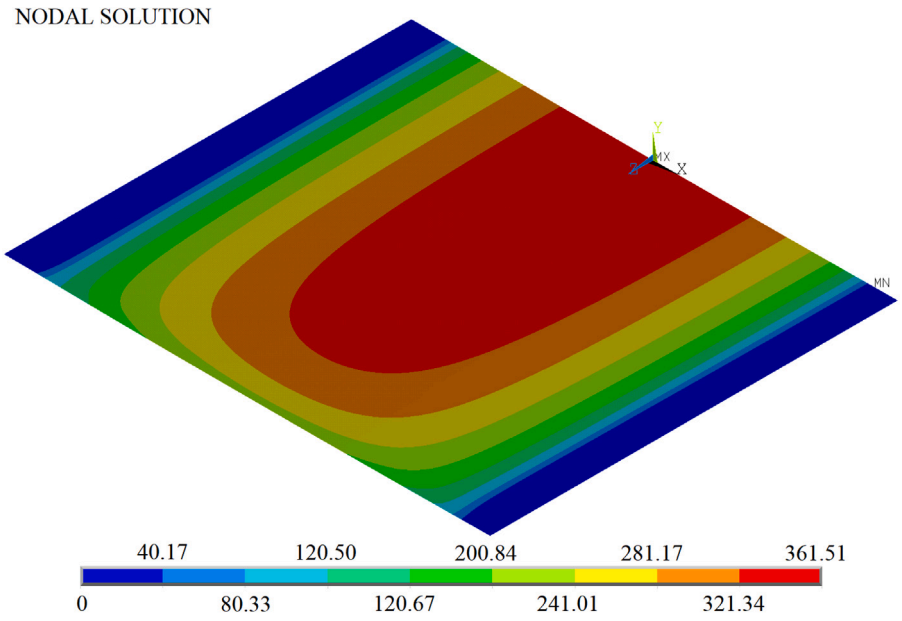

Fig. 5. Contact pressure distribution, $\left|\sigma_{yy}(x,0,z)\right|$, over test specimen in configuration 1.

Table 2
Geometric dimensions for the FEM models.

a	R	l	h_p	h_t	w_t
1.8mm	100mm	$20a$	$10a$	$10a$	$4a$

fillet is also included to avoid a theoretically, and unrealistic, infinite stress raiser.

3.1. FEM models

Even for the simplest case analysed here, case shown in Fig. 3a.1, there is no 3D analytic solution, therefore a numerical model is required in order to study the behaviour of the fretting tests considered here. In this paper all analyses have been performed without a bulk stress, because in the present work we are focused on the effects produced by the geometry of test specimen and contact pad on the surface stress field, and it is thought that the effect due to this bulk stress is not relevant. In all cases the applied total normal load, N, produces an average load per unit length (line load), $N^* = 1000$ N/mm, and the total tangential load is always $Q = 0.75$ μN; values that are representative of usual fretting tests. Regarding the geometry, in all cases the pad radius is $R = 100$ mm, the height of test specimen and contact pad, h_t and h_p respectively (see Fig. 3), are set to ten times ($10a$) the Hertzian contact semi-width under plane strain conditions; $a = 1.80$ mm in the present case, and the width of the test specimen in the contact zone, w_t, is set equal to $4a$. In addition, and to avoid size effects in the modelling, the length of test specimen, l, and contact pad is set to $20a$. As a summary, Table 2 shows the leading geometric dimensions used in the FEM models. It is important to note that the geometric dimensions has been chosen taking into account that the specimen width is sufficiently large in comparison with the contact width. In this sense, the use of larger dimensions should not influence the results. This is not the situation for cases having a specimen width similar or smaller than the contact width, since in these cases results would tend to a stress state similar to that of plane stress.

The commercial software ANSYS has been used to simulate the mechanical behaviour of all contact pairs. As stated above, we are focused on the effects produced by the geometry of test specimen, and for this reason a linear elastic material behaviour is considered for both, the contact pad and test specimen; although an elastic–plastic model can be considered, the different results between geometries are better analysed with a linear elastic behaviour. Furthermore, it is quite common for fretting tests to be carried out under high cycle fatigue regime, and thus under elastic behaviour. The elastic modulus (Young's modulus) and Poisson's ratio are $E = 70$ GPa and $\nu = 0.33$ respectively, and thus resembling the case in which the raw material of the contact pair is an aluminium alloy. A linear formulation for the solid elements has been considered. The submodelling technique is used to obtain a very precise contact solution over the contacting areas. In the submodel the mesh density, especially at the contact zone, is fine enough to capture the stress gradients in the contact region; the minimum element size is approximately 4.0 μm. With this mesh size, a convergence in the peak value for the direct stress σ_{xx} at the contact surface was achieved. We decided to use the direct stress σ_{xx} because it presents a very steep gradient at the contact trailing edge, and thus is a good benchmark for the convergence. For all test configurations two submodels were used: one to analyse the near front part ($z = w_t/2$) and another for the analysis of near middle-width section part ($z = 0$). A scheme of the model, for the case in which $w_t = w_p$, and a view of the meshes, coarse and fine models (front part submodel in the present figure), is shown in Fig. 4a. Due to symmetry considerations (about $z = 0$ plane), only half of the complete geometry is modelled. Fretting loads, N and Q, are applied remotely on the pad top surface via a master node. The test specimen bottom surface is clamped, and because the height of this part ($10a$) is large enough, this boundary condition does not affect the results obtained at the contact zone. In all cases, first the normal load is sequentially applied up to its maximum value, then this value is kept constant, and finally the tangential load is sequentially applied up to its maximum value. As shown in Fig. 4b, both normal and tangential load are applied by consecutive steps. Each step load is divided in 10 substeps, so that the load is increased by a factor of 1/10 of its final value between consecutive substeps. In addition, the time increment in each substep is equal to 0.0025. The contact algorithm used in the simulations is the Augmented Lagrangian Method, which produces a good ratio between accuracy and CPU times. According to experimental values [28], the coefficient of friction, μ, has been fixed equal to 0.7, a high value that makes necessary the use of an unsymmmetric iterative solver in order to achieve numerical convergence. Finally, in all the FEM models the CPU time was around 2 h in a computer with 12 cores (3.7 GHz) and 64 GB of RAM.

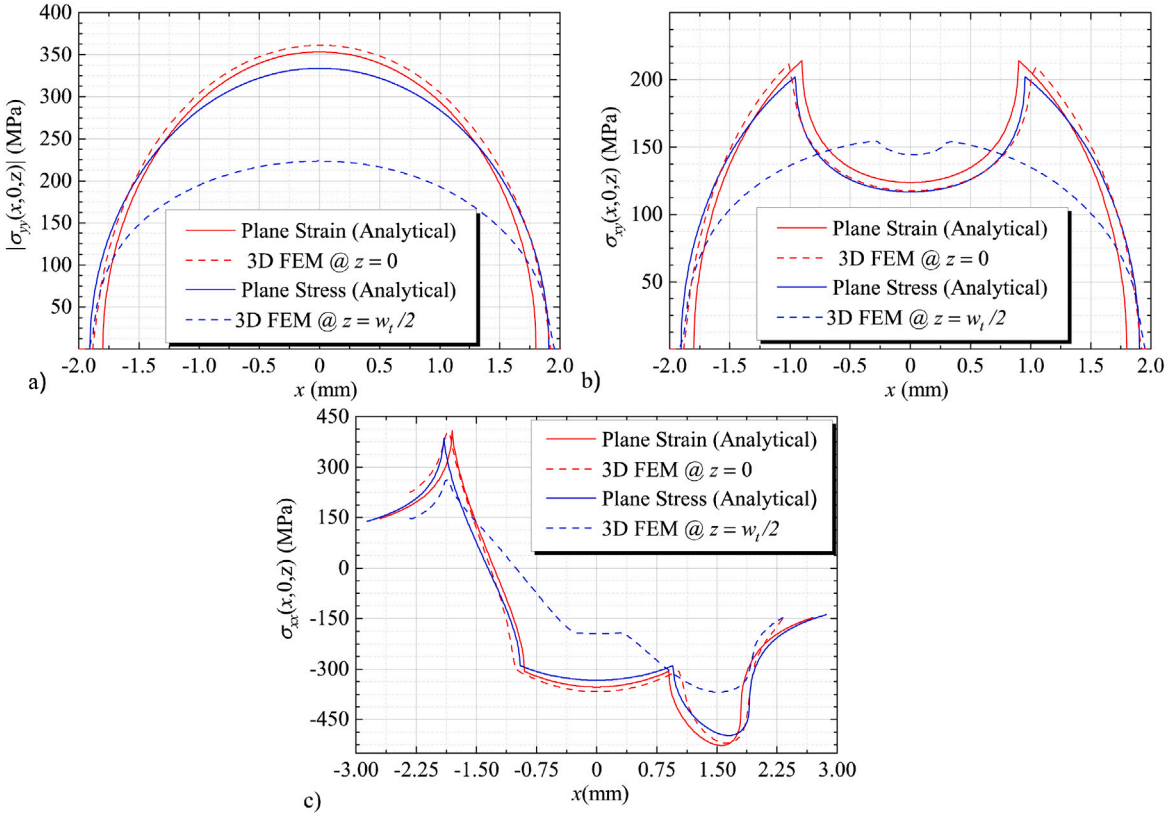

Fig. 6. (a) Surface contact stress, $\sigma_{yy}(x)$, for 2D models and at two sections ($z = 0$ and $z = w_t/2$) of the test specimen (3D FEM), (b) Surface contact stress, $\sigma_{xy}(x)$, for 2D models and at two sections ($z = 0$ and $z = w_t/2$) of the test specimen (3D FEM), (c) Surface direct stress, $\sigma_{xx}(x)$, for 2D models and at two sections ($z = 0$ and $z = w_t/2$) of the test specimen (3D FEM).

Table 3
Specific FEM parameters.

	Configuration 1	Configuration 1.1	Configuration 2	Configuration 3
w_p	$4a$	$4a$	$8a$	$4a$
$N^1(N)$	$N^* \frac{w_t}{2}$	$N^* \left(\frac{w_t}{2} - r\right)$	$N^* \left(\frac{w_t}{2} - r\right)$	$N^* \frac{w_t}{2}$
$N^*(N/mm)$	1000	1000	1000	1000
r	0	$0.1a$	$0.1a$	0

N^1 Normal load applied to the FEM model considering symmetry

Following, the analysis and discussion of the configurations here considered are shown. Finally, and although in next sections a complete explanation of the different configurations will be shown, Table 3 shows the specific parameters, loading and geometric, for each of the cases here analysed, with the aim to easily compare the differences between the simulated cases.

3.2. Configuration 1. Contact pad and test specimen having the same width ($w_p = w_t$)

The geometries of the contact pad and test specimen considered in this section are shown in Fig. 3a.1. In this case, and to have a complete visualisation of the stress field on the test specimen contact area, a complete model with a fine mesh at the contact zone has been solved; the features of this model are the same to that mentioned above for the coarse model and submodel. Fig. 5 shows the absolute value of the contact pressure distribution, $|\sigma_{yy}(x,0,z)|$, obtained on the test specimen surface with the complete model at step 2; unless stated otherwise, this is the time step used along all the text. In this picture we can observe the notable variation of the contact pressure with the z-coordinate, showing that the maximum contact pressure is obtained at $z = 0$ (middle-width plane). This fact by itself could justify a different fretting fatigue behaviour between the outer plane ($z = w_t/2$) and the middle-width plane. The physical insight of this assertion, lies in the above results which indicate a notable different normal stiffness at $z = 0$ and $z = w_t/2$, and thus a similar variation of the tangential stresses is expected.

Fig. 6a to c shows the contact stress distribution, $|\sigma_{yy}(x)|$ and $\sigma_{xy}(x)$, and the direct stress, $\sigma_{xx}(x)$, obtained via submodels at test specimen's sections $z = 0$ and $z = w_t/2$. In addition, and for comparison purposes, these figures also show the corresponding theoretical (Hertzian) 2D stress distribution (assuming plane stress and plane strain behaviour) obtained with $N^* = 1000$ N/mm and $Q^* = 0.75$ μN*; the analytical equations for these stresses can be obtained elsewhere [31]. A remarkable fact in this figure, although already shown in Fig. 5, is the difference between the contact pressure distributions obtained at $z = w_t/2$ and $z = 0$; the ratio between the maximum values found at $z = 0$ and $z = w_t/2$ is about 1.6. In addition, and when comparing results between Figs. 5 and 6a, it is noteworthy that both the complete model and submodels produce nearly the same peak values in the contact normal stress σ_{yy}. On the other hand, it is observed that for $z = 0$ the contact pressure distribution is quite similar to that obtained with the theoretical 2D plane strain model, which is in line with expectations. Meanwhile, a quite different behaviour is obtained at $z = w_t/2$, being

the 3D pressure distribution far below its expected counterpart 2D solution (plane stress). These results show that the normal load is not uniformly distributed along the test specimen's width (z-coordinate), being this proportion higher in the middle section ($z = 0$) and lower at the surface ($z = w_t/2$). In addition, Fig. 6a shows that the contact sizes obtained with the numerical model are very close to that obtained analytically, especially when plane stress is assumed; the contact semi-width assuming plane stress behaviour is $a^* = 1.90$ mm. In relation to the 3D surface shear stress, σ_{xy}, Fig. 6b shows the distributions obtained at $z = 0$ and $z = w_t/2$. It is important to note that σ_{xy} distributions for plane strain and 3D FEM at $z = 0$ are quite similar, although a wider stick zone is predicted by FEM. On the contrary, 3D FEM σ_{xy} distribution at $z = w_t/2$ shows the lowest values and the smallest stick zone. Such a shear stress distribution is expected in view of the normal pressure distribution obtained at $z = w_t/2$ with the FEM model. The small stick zone predicted by FEM at $z = w_t/2$ may be attributed to the manner in which the tangential load is distributed along the z-coordinate, which should be different to that of the normal load and thus producing a $Q^*/\ \mu N^*$ ratio different from 0.75. Finally, Fig. 6c shows the surface direct stress σ_{xx}; distributions obtained via 3D FEM and those produced with 2D models are plotted together for comparison. This figure shows that 3D results at $z = 0$ are very close to those obtained with 2D models, especially assuming plane strain behaviour. On the other hand, the results at $z = w_t/2$ are far from those obtained with bi-dimensional models, but in agreement with the normal and shear contact stress obtained via FEM at $z = w_t/2$; see for example that at $z = w_t/2$ the extension of the nearly flat portion in σ_{xx} coincides with the stick zone obtained in the σ_{xy} distribution. In all numerical cases the peak direct stress is produced at the contact trailing edge, place where the value of direct stress σ_{xx} is only due to the surface shear stress distribution, as no bulk stress is considered in the simulations. Note that σ_{xx} peak values at $z = 0$ and $z = w_t/2$ are 388 MPa and 259 MPa respectively, and based on this crack initiation is likely to occur at $z = 0$. However, the normal pressure distribution shown in Fig. 5, suggests that a significant portion of the test specimen width must be subjected to a direct stress distribution similar to that obtained at $z = 0$, suggesting that fretting cracks would initiate along a big portion of the contact trailing edge. These results are in agreement with the experimentally observed behaviour in a previous authors' work [76], in which almost simultaneously many cracks initiate along the contact trailing edge.

All the results shown above invite to analyse the manner in which the normal and tangential load are distributed along the test specimen width. It is possible to obtain the variation for N^* and Q^* over the test specimen semi-width by integrating the normal and shear contact stress distribution, $\sigma_{yy}(x)$ and $\sigma_{xy}(x)$, with respect to the x-coordinate at different z values. These results are shown in Fig. 7 as $N^*(z)$ and $Q^*(z)$. Firstly, notice how different is the variation of $N^*(z)$ and $Q^*(z)$ with respect to z; the first one presents an important decrease for $z/(w_t/2) > 0.5$, meanwhile $Q^*(z)$ is roughly constant up to a value of $z/(w_t/2) = 0.94$, indicating that the contact normal stiffness is strongly affected by the 3D behaviour but not so much the tangential stiffness. In view of these curves, it is expected that crack initiation would likely occur first in the contact trailing edge between $z/(w_t/2) = 0.5$ and $z/(w_t/2) = 0.9$, approximately (region with a grey crossing pattern); area where $N^*(z)$ decreases rapidly but $Q^*(z)$ maintains its value. It is known that, for the same Q^*, a higher value of N^* delays the fretting crack initiation process [12,57,76]. Also, note that close to $z \approx 0$, $N^*(z) > 1000$ N/mm (the reference value), and it explains by itself the differences obtained in Fig. 6a between the theoretical (plane strain behaviour) and FEM (at $z = 0$) stress distributions. In addition, and in view of the value of $N^*(w_t/2)$, a similar explanation can be given for the differences at $z = w_t/2$ between the theoretical (plane strain or plain stress behaviour) and FEM normal pressure distributions. Regarding the tangential loading, the value for $Q^*(w_t/2)$ and $N^*(w_t/2)$ explain the surface contact shear stress distribution obtained via FEM at $z = w_t/2$. In addition, it is found that for $z = 0$ the tangential line load value is $Q^* = 530.0$ N/mm, a very similar value to the reference value of 525 N/mm (0.75 μN^*). To complete the analysis, the fretting load ratio, $Q^*(z)/(\mu N^*(z))$, is shown in Fig. 7, which depicts that this ratio is very close to the reference value of 0.75 up to a width of $z/(w_t/2) \approx 0.75$. Then this ratio increases rapidly with z up to a value very close 1.0, and thus explaining the small stick zone obtained by FEM at $z = w_t/2$.

Finally, to deepen in the knowledge of the 3D behaviour and how it affects the contact stress field, the values obtained from the FEM analysis for $N^*(z)$ and $Q^*(z)$ at $z = 0$ and $z = w_t/2$ have been used to recalculate the corresponding 2D analytical surface contact stress distributions. These distributions have been obtained assuming plane strain for $z = 0$ and plane stress for $z = w_t/2$. The results are depicted in Fig. 8, and show that now 3D FEM distribution obtained at $z = 0$ and those assuming plane strain conditions, are nearly the same and with only a slight difference at the contact edges. On the other hand, FEM results obtained at $z = w_t/2$ differ notably with those obtained assuming plane stress behaviour; in view of the plots shown in Fig. 8 similar results are expected if plane strain behaviour is considered. Nonetheless, and surprisingly, both models, plane stress and FEM at $z = w_t/2$, virtually produce the same stick zone length.

Finally, the above results indicate that in the middle-width section ($z = 0$), and when properly selected the line loads N^* and Q^*, the surface contact stress distributions can be accurately predicted assuming the theoretical plane strain solution. In contrast, the mechanical behaviour at $z = w_t/2$ (and likely at sections near the free surface defined by $z = w_t/2$) greatly differ to that obtained by using plane stress or plane strain theoretical solutions.

3.2.1. *Configuration 1.1. $w_p = w_t$ but test specimen having a fillet*

Now the pad and test specimen geometries are those shown in Fig. 3a.2. In the case analysed here test specimen and contact pad have a fillet with a radius, $r_{fillet} = 0.1a = 0.18$ mm, which is a feasible value after a typical machining process. In order to apply a total normal load, N, producing a value of N^* close to 1000 N/mm, and thus making this analysis comparable with that shown above, N has a value equal to $N^*(w_t/2 - r_{fillet})$; we selected this value because FEM results showed that only a minor area of the fillets come into contact. In the present geometry, a complete model having a resolution high enough to properly capture the stress gradient present at the fillets is out of our CPU capabilities. In any case, Fig. 9a shows the contact pressure distribution at test specimen's surface obtained with the coarse (complete) model, in which it is observed that a maximum value of 366.38 MPa is produced close to the fillet edge.

For a better analysis of the contact stress distributions at the fillet, more precise results have been obtained via submodelling. For completeness, Fig. 9b shows the surface normal pressure obtained near the filleted zone. Fig. 10 shows the $|\sigma_{yy}(x,0,z)|$, $\sigma_{xy}(x,0,z)$ and $\sigma_{xx}(x,0,z)$ distributions obtained with the submodels at $z = 0$ mm and $z \approx 0.94 w_t/2 = 3.39$ mm, being this last location the place where the maximum normal contact pressure (602.71 MPa) has been found. Additionally to the FEM results, and for the sake of clarity, in this figure only theoretical stress distributions corresponding to plane strain behaviour have been included. Similarly to the previous case, stress distributions obtained at $z = 0$ are very close to those obtained assuming plane strain behaviour. On the other hand, the contact stress distributions $|\sigma_{yy}(x)|$ and $\sigma_{xy}(x)$ obtained at $z = 3.39$ mm, are far from those at the middle-width section; see for example the big difference between the peak values for σ_{yy} at $z = 3.39$ and $z = 0$. Regarding the direct stress, σ_{xx}, values near the filleted zone are lower than values at $z = 0$. We can see that the difference between the maximum peak values at $z = 3.39$ and $z = 0$ is roughly 100 MPa, a difference similar to that previously found in the case without fillets. In view of the shear stress distribution obtained at $z = 3.39$ mm, a higher difference between these σ_{xx} peak values would be expected, a fact that can be only attributed to the especial 3D behaviour provided by the fillet.

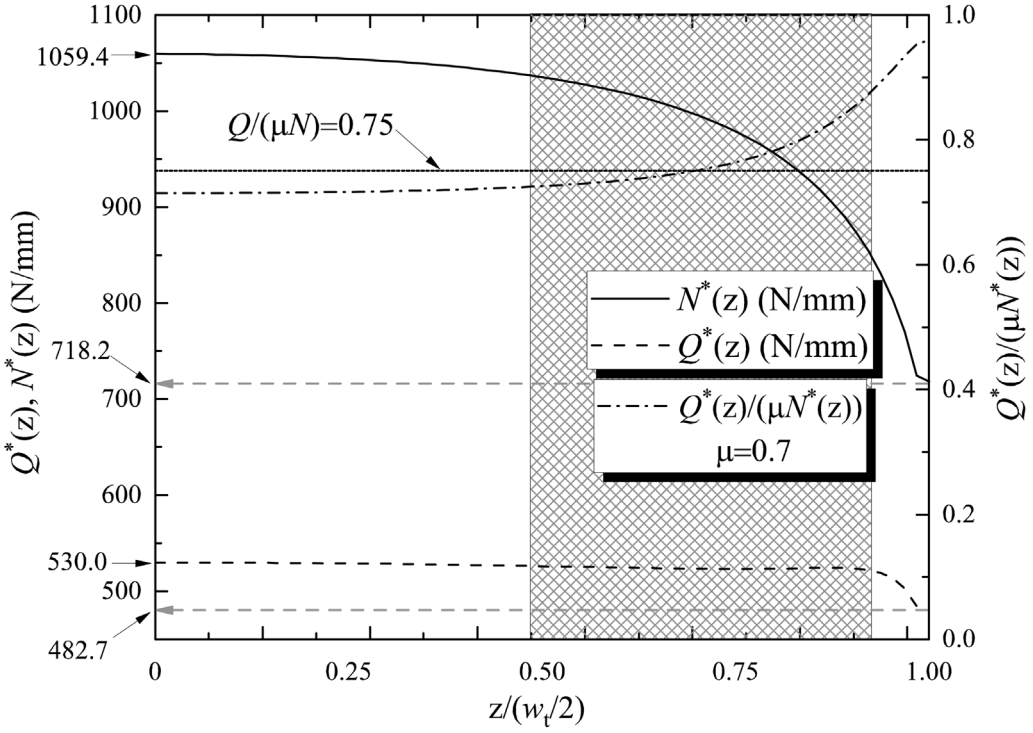

Fig. 7. Variation of $N^*(z)$ and $Q^*(z)$ and fretting load ratio $Q^*(z)/(\mu N^*(z))$ along the test specimen's width.

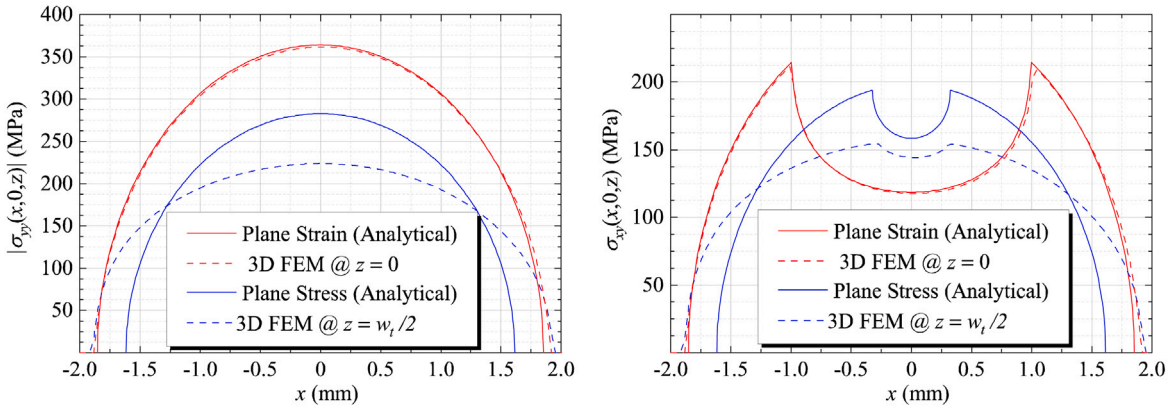

Fig. 8. Comparison of 3D FEM contact stress distribution with the corresponding 2D theoretical ones (plane stress and plane strain) but using the values of $N^*(z)$ and $Q^*(z)$ obtained at $z = 0$ and $z = w_t/2$.

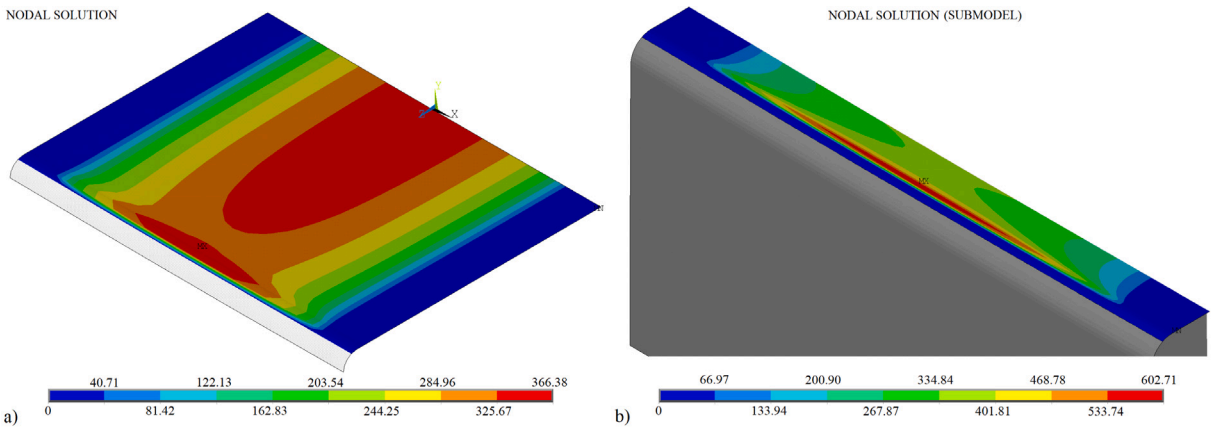

Fig. 9. (a) Surface contact stress $|\sigma_{yy}(x,0,z)|$ obtained with the coarse model in the case of geometries with fillets, (b) Surface contact stress $|\sigma_{yy}(x,0,z)|$ obtained with the submodel near the fillet.

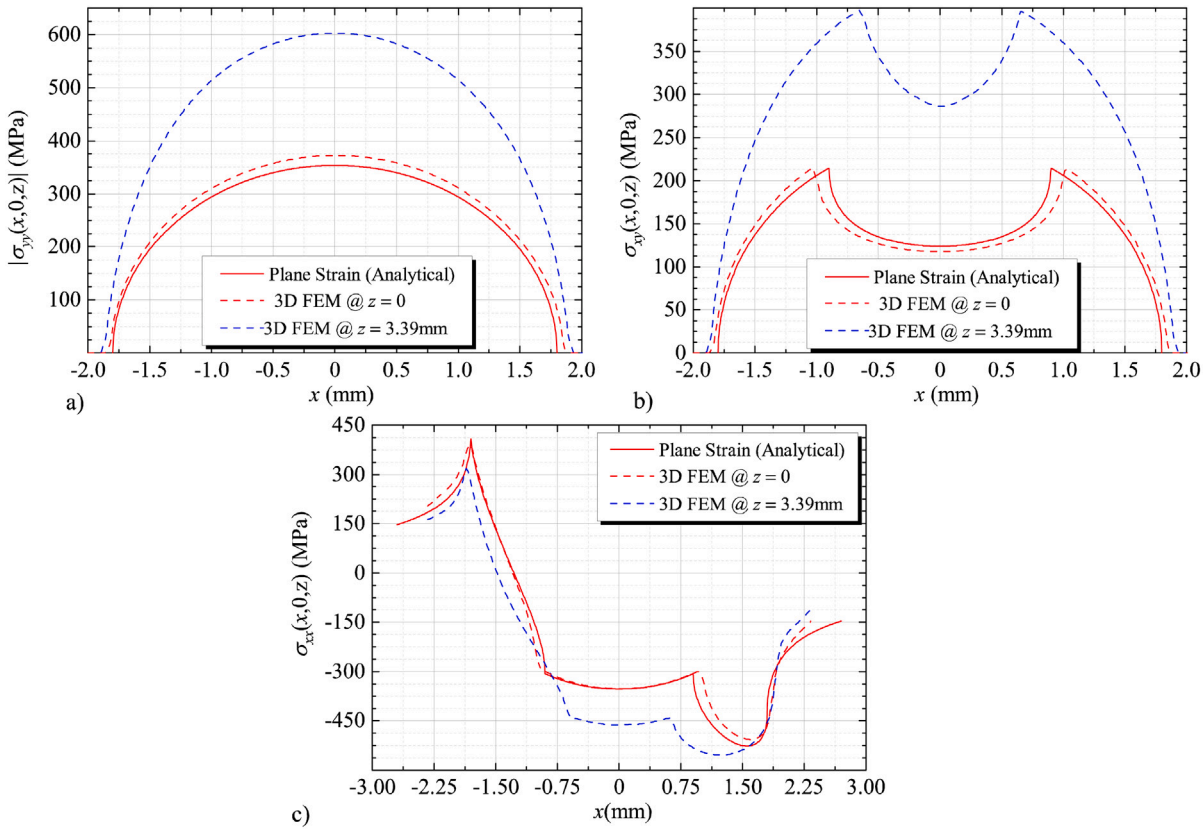

Fig. 10. (a) Surface contact stress, $\sigma_{yy}(x)$, for 2D model (plane strain) and at two sections ($z = 0$ and $z = 3.39$ mm) of the test specimen (3D FEM), (b) Surface contact stress, $\sigma_{xy}(x)$, for 2D model (plane strain) and at two sections ($z = 0$ and $z = z = 3.39$ mm) of the test specimen (3D FEM), (c) Surface direct stress, $\sigma_{xx}(x)$, for 2D model (plane strain) and at two sections ($z = 0$ and $z = z = 3.39$ mm) of the test specimen (3D FEM).

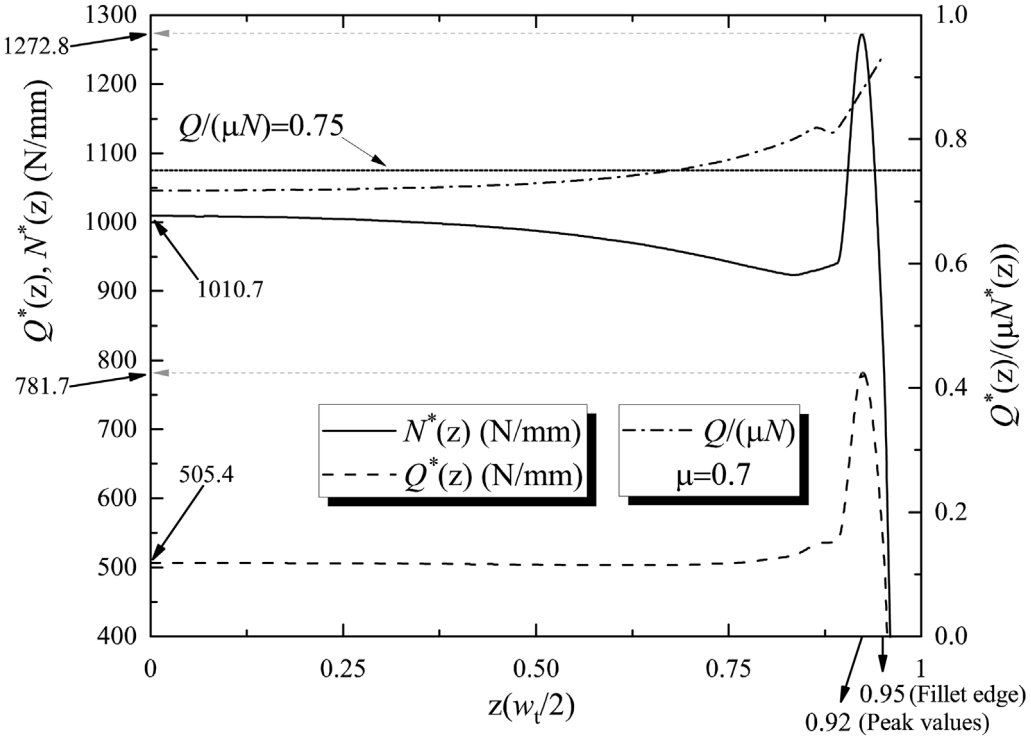

Fig. 11. Variation of $N^*(z)$ and $Q^*(z)$ and fretting load ratio $Q^*(z)/(\mu N^*(z))$ along test specimen's width in the case with a fillet.

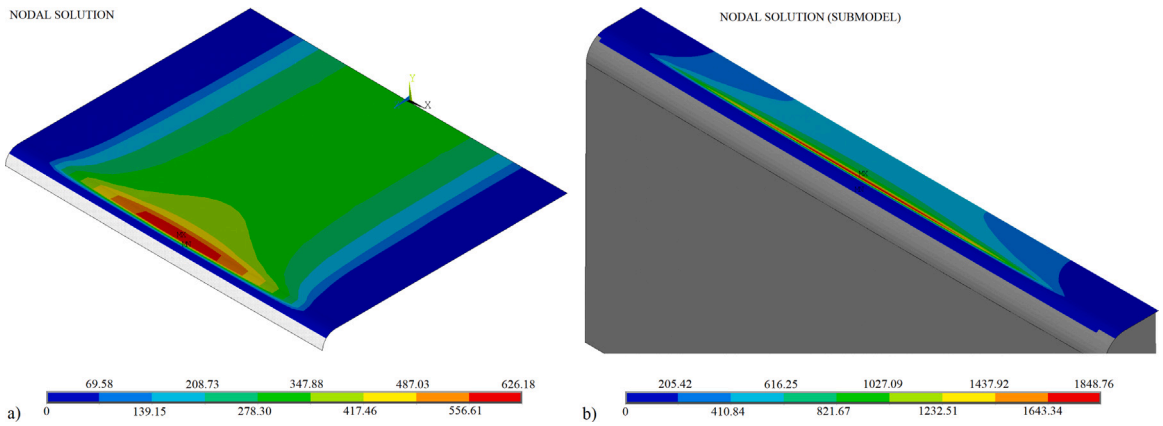

Fig. 12. (a) Surface contact stress $\left|\sigma_{yy}(x,0,z)\right|$ obtained with the coarse model in the case of $w_p = 2w_t$, (b) Surface contact stress $\left|\sigma_{yy}(x,0,z)\right|$ obtained with the submodel in the case of $w_p = 2w_t$.

Fig. 11 shows the line load distributions $N^*(z)$ and $Q^*(z)$ for the case with a fillet (using the complete FEM model), which clearly shows that the fillet acts as a stress concentrator. Now the line loads values at $z = 0$ are fairly the same to that corresponding to reference values (1000 N/mm and 525 N/mm, respectively), but near the fillet edge $(z/(w_t/2) = 0.95)$ there are high line load values; exactly at $z \approx 0.92w_t/2 = 3.31$ mm are the maximum increments with respect to the reference values. These increments are about 27% and 49% for the normal and tangential line loads, respectively.

In relation with last comment, Fig. 10c shows that the direct stress, σ_{xx}, peaks at $z = 0$, so it might be thought that this is the place prone to crack initiation, but in the fretting crack initiation process not only the peak value matters, also the extension of the contact stress field is important, and higher $N^*(z)$ and $Q^*(z)$ values implies that the contact stress field extends with notable values at higher depths, and thus leading to a high crack initiation probability [77,78]. In any case, in order to obtain firmer conclusions a detailed analysis of the stress/strain gradients at those zones need to be performed by means of a suitable fatigue model [29,30,79].

Finally, and on the basis of the above fact, it is worth noting that crack initiation at the test specimen corner's section is an undesirable fact, specially if the bulk material behaviour against fretting is going to be obtained from tests; material's modification produced by surface treatments like shot peening, laser peening, carburising or nitriding can be different at test specimen corner's section to that produced far from it.

3.3. Configuration 2. Contact pad having a width longer than test specimen ($w_p > w_t$)

The arrangement for this case is shown in Fig. 3b. Now contact pad's width is twice the test specimen width, i.e., $w_p = 8a$. In this configuration test specimen having a fillet with a radius $r_{fillet} = 0.1a$ is considered directly, because if such a feature is not included unrealistic contact stresses will be obtained at the contact edges located at $z = \pm w_t/2$; theoretically the contact stresses at these edges tend to infinity. In the configuration here analysed the normal stiffness of the contact pad, specially at zones near $z = w_t/2$, is clearly higher than the test specimen one, and thus leading to a considerable stress raiser in those zones. This effect can be seen in Fig. 12a, where the absolute value of the normal contact stress distribution obtained with the coarse model, $\left|\sigma_{yy}(x,0,z)\right|$, is plotted. Here the behaviour, although not quantitatively, is qualitatively similar to the case shown in the previous section; again the maximum value is produced at the fillet edge, but now, and comparing results provided by coarse models, this maximum σ_{yy} value is remarkably higher (626.18 MPa) than the previous value of 366.38 MPa, as expected. In addition, a similar plot is shown in Fig. 12b, but now with the submodel which is used for a detailed analysis of the contact pair near the fillet. Note the difference between the maximum normal pressure obtained with the coarse model and that with the submodel near the fillet edge, which is 3 times larger; 626.18 MPa vs. 1848.76 MPa.

The analyses done with the corresponding submodels, give that both the maximum pressure and maximum direct stress, σ_{xx}, is obtained at the section located at $z = 3.42$ mm; a very close location to that previously found in the above section. Fig. 13 shows the contact stress distributions and the direct stress at $z = 0$ mm and $z \approx 0.95w_t/2 = 3.42$ mm. In this figure, at $z = 3.42$ mm and around the middle of the contact zone $(z \approx 0)$, $\sigma_{yy}(x)$ has a flat as well as a small eccentricity in its distribution at the loading step 2, and therefore being far from an elliptical traction distribution. In addition, Fig. 13a shows the pressure distribution at time step $t = 1$ s (that is, with only normal load) and at $z = 3.42$ mm, in which no eccentricity is observed, indicating that this feature appears when the tangential load is applied and is due to the difference between the tangential stiffnesses of contact pad and test specimen produced by the highly 3D stress state. Regarding the contact surface shear stress, $\sigma_{xy}(x)$, Fig. 13b shows the distributions obtained in the present case. First, we note that for $z = 3.42$ mm the numerical solution is not as smooth as those previously obtained, the reason is a numerical problem, due to excessive penetration produced during the numerical solution and that issue is quite difficult to overcome; an increase in the normal stiffness of the contact element reduces penetration but leads to convergence difficulties. In Fig. 13b, it is also visible the eccentricity at $z = 3.42$ mm, which leads to a non-central stick zone. Fig. 13c shows $\sigma_{xx}(x)$ distributions, in which readily it is observable a non-negligible increment of roughly 50 MPa when compared with the previous cases here analysed. Finally, stress distributions obtained at $z = 0$ mm are nearly the same to that obtained in above sections.

The analysis for the line load distributions is shown in Fig. 14. This figure shows that $N^*(z)$ and $Q^*(z)$ at $z = 0$ are roughly a 10% less than the reference values ($N^* = 1000$ N/mm and $Q^* = 525$ N/mm). Again near the fillet edge, at $z/(w_t/2) \approx 0.92$, it is found the highest line load values. A huge increment of about a 202% and 170% with respect to the reference values is produced for the normal and tangential line loading respectively. Therefore, and similarly to the previous case, but here more clearly because also σ_{xx} peaks close to $z/(w_t/2) \approx 0.92$, all these data indicate that this z-location is the place where almost certainly fretting cracks initiation will occur.

3.4. Configuration 3. $w_p = w_t$ at contact zone, but test specimen having a variable width

Fig. 3c shows a scheme for the configuration here analysed. In this case the FEM model resembles the contact pair shown in Fig. 3c, and we

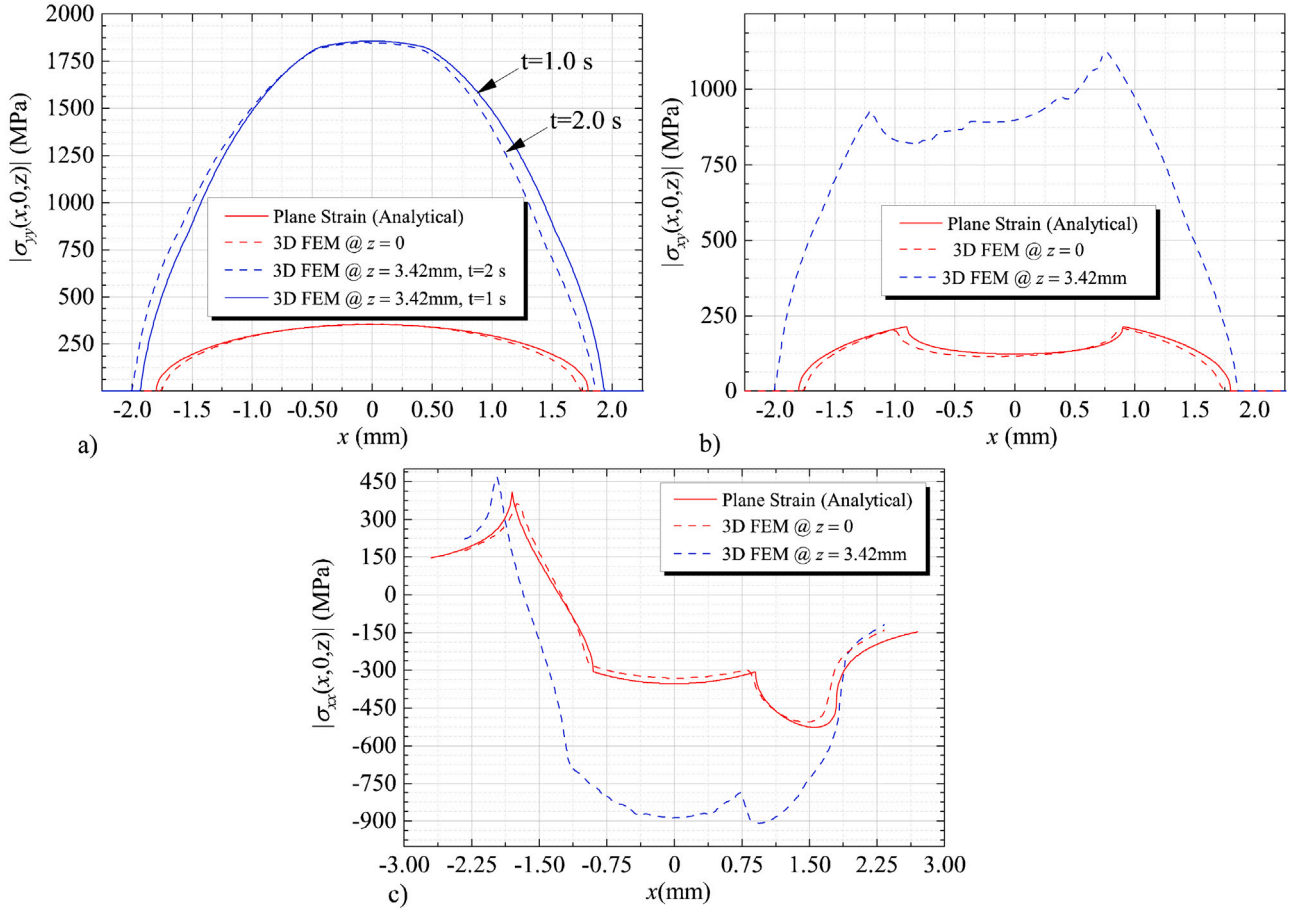

Fig. 13. (a) Surface contact stress, $\sigma_{yy}(x)$, for 2D model (plane strain) and at two sections ($z = 0$ and $z = 3.42$ mm) of the test specimen (3D FEM), (b) Surface contact stress, $\sigma_{xy}(x)$, for 2D model (plane strain) and at two sections ($z = 0$ and $z = z = 3.42$ mm) of the test specimen (3D FEM), (c) Surface direct stress, $\sigma_{xx}(x)$, for 2D model (plane strain) and at two sections ($z = 0$ and $z = z = 3.42$ mm) of the test specimen (3D FEM).

use "resemble" because the model is not exactly that depicted in such a figure, its actual geometry corresponds to that shown in Fig. 15a. We use that model, because near the contact zone the geometry is identical to that of Fig. 3c. However, and similarly to preceding cases, the height and width of the test specimen is set equal to $10a$ and $2a$ respectively in order to avoid size effects, and thus making possible the comparison with previous cases. The radius of the test specimen's section having a circular part is set equal to $2/3w_p$, a similar proportion to that found in the works marked as f1 in Table 1. Prior to displaying the contact stress field obtained in the present case, we note that in the contact stick zone the mechanical behaviour of the contact pair must be similar to that of a reentrant wedge, i.e. having an angle less than 180°. In the present case the angle is equal to 135° (see Fig. 14b) and thus theoretically a singular normal contact stress behaviour with a strength of the order of $r^{-0.325}$ is expected [80].

To have a global and local picture of the contact pressure, Fig. 16a and 16b show the normal contact stress distributions obtained with the full model (coarse) and the submodel respectively. As predicted above, this figure shows that a notable stress raiser is produced near $z = w_p$. All the surface stress distributions obtained using the submodelling technique at $z = w_t/2$ and $z = 0$ are shown in Fig. 17. First, note that at $z = w_p/2$ the shape (not the maximum values) for $\sigma_{yy}(x)$ and σ_{xy} distributions are similar to those previously shown in Fig. 13a and b, but now the eccentricity in both distributions is to the right because in this case the element with the highest contact stiffness is the test specimen. In the above case the contact pad was the element with the highest contact stiffness. On the other hand, it is quite surprising that the peak value for $\sigma_{xx}(x)$ at $z = w_p/2$ is lower to that produced at $z = 0$.

Finally, Fig. 18 shows the line loads $N^*(z)$ and $Q^*(z)$ distribution along the test specimen's width, in which it is observed that along a great extension of the test specimen's width the line loads values are nearly similar to the references values, and then raise with a steep gradient when approaching to $z = w_p/2$ and thus promoting the fretting crack initiation at that zone, a fact that can be observed in some of the fractographies shown in [70].

3.5. Subsurface fatigue behaviour for the configurations

Previous sections analyse and discuss about the contact stress distributions at the contact surface and, independently of the test configuration, a noticeable difference is observed depending on the position along the test specimen thickness at which surface contact stresses are evaluated. However, fatigue phenomenon, and in particular fretting fatigue, requires a deeper analysis taking into account what happens in the very near subsurface material – process zone – since the initiation and early growth of fretting cracks is a process that will depend on what happens in that process zone. Therefore, for a deeper comprehension it is necessary to carry out an analysis below the contact surface in order to assess the more prone place for a possible crack initiation along the test specimen thickness and its subsequent fatigue crack growth. This section deals with this objective assuming that cracks initiate at the trailing edge.

First, and in order to analyse the crack nucleation behaviour, a plane containing the trailing edge and perpendicular to the contact surface is analysed in terms of the direct/axial alternating stress, σ^a_{xx}, produced during a cycle in which tangential load Q is fully reversed ($R_Q = -1$).

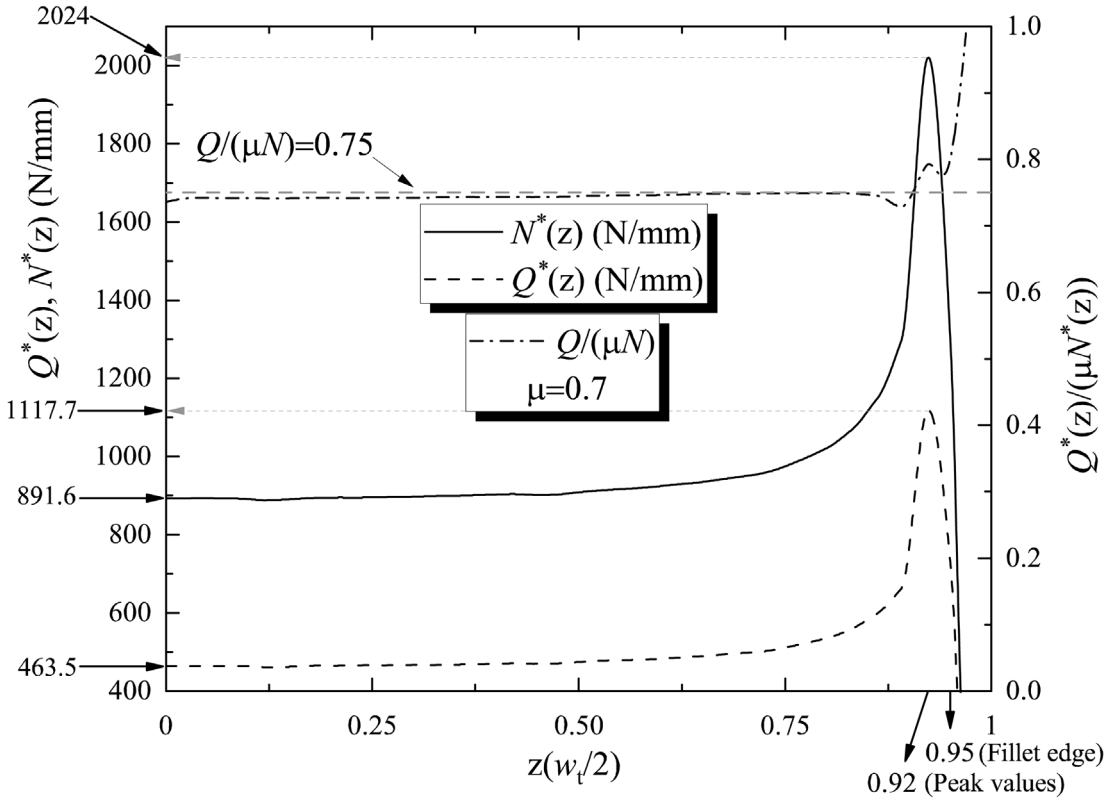

Fig. 14. Variation of $N^*(z)$ and $Q^*(z)$ and fretting load ratio $Q^*(z)/(\mu N^*(z))$ along test specimen's width in the case of $w_p = 2w_t$.

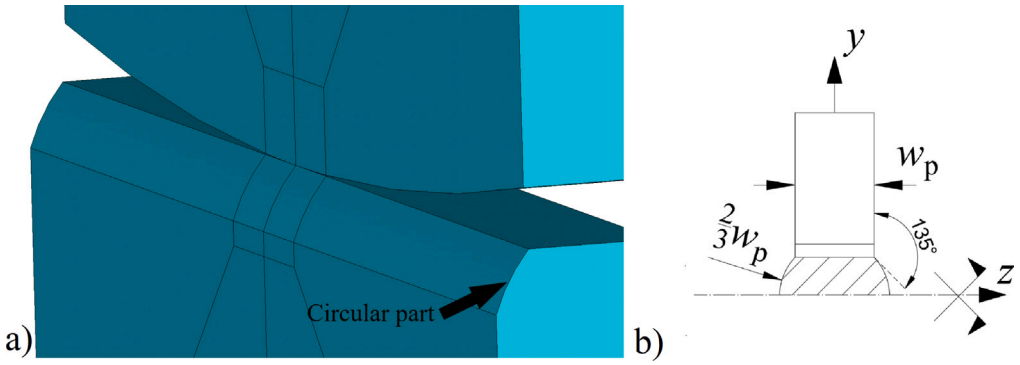

Fig. 15. (a) FEM model used to analyse the behaviour of type f1 tests, (b) Tangent angle between pad and test specimen.

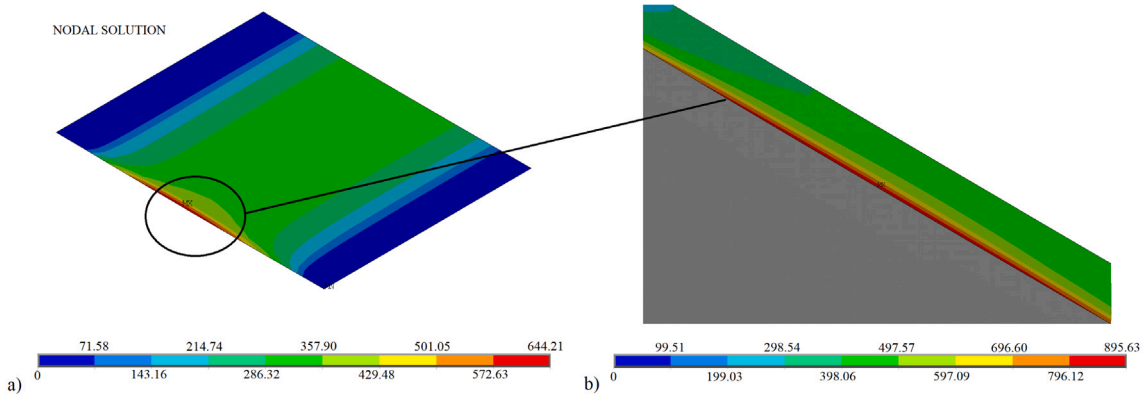

Fig. 16. (a) Surface contact stress $\left|\sigma_{yy}(x,0,z)\right|$ obtained with the coarse model in the case $w_p = w_t$ at contact zone, but test specimen having a variable width, (b) Surface contact stress $\left|\sigma_{yy}(x,0,z)\right|$ obtained with the corresponding submodel.

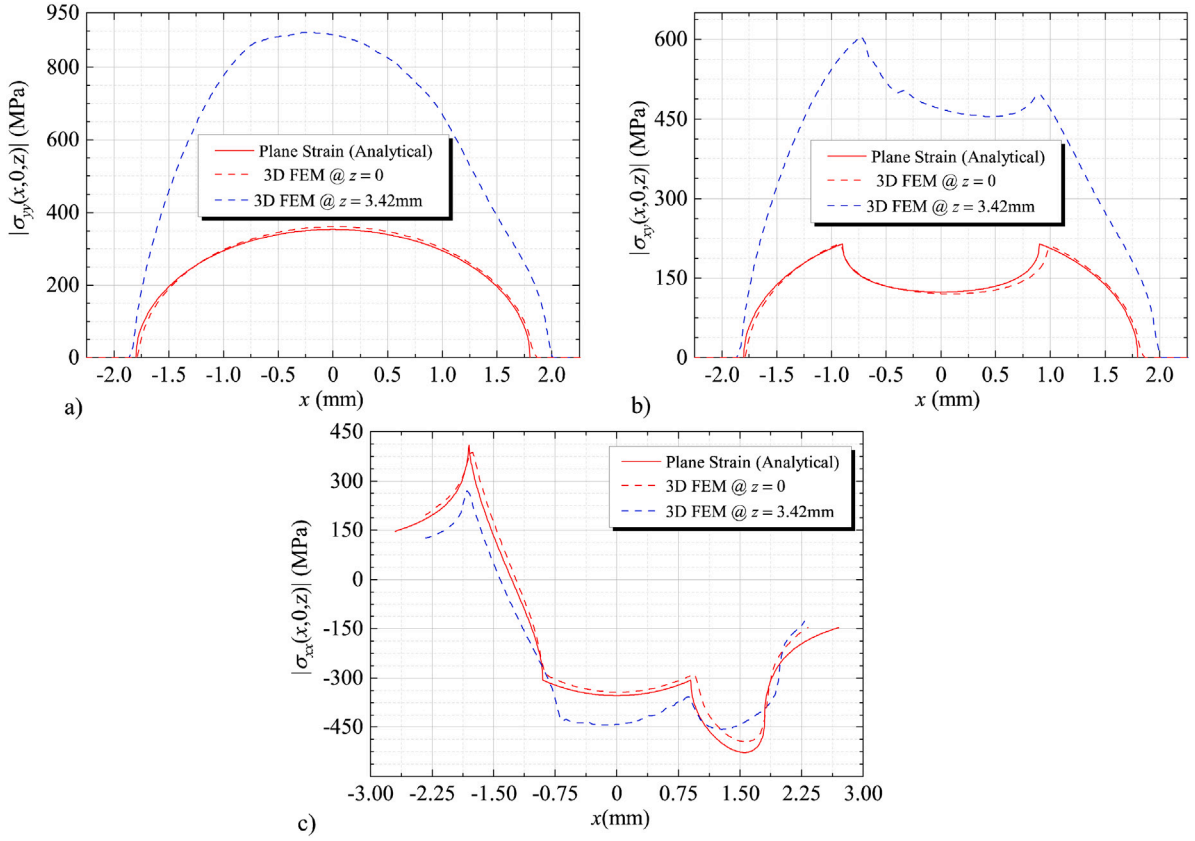

Fig. 17. (a) Surface contact stress, $\sigma_{yy}(x)$, for 2D model (plane strain) and at two sections ($z = 0$ and $z = w_p/2$) of the test specimen (3D FEM), (b) Surface contact stress, $\sigma_{xy}(x)$, for 2D model (plane strain) and at two sections ($z = 0$ and $z = w_p/2$) of the test specimen (3D FEM), (c) Surface direct stress, $\sigma_{xx}(x)$, for 2D model (plane strain) and at two sections ($z = 0$ and $z = w_p/2$) of the test specimen (3D FEM).

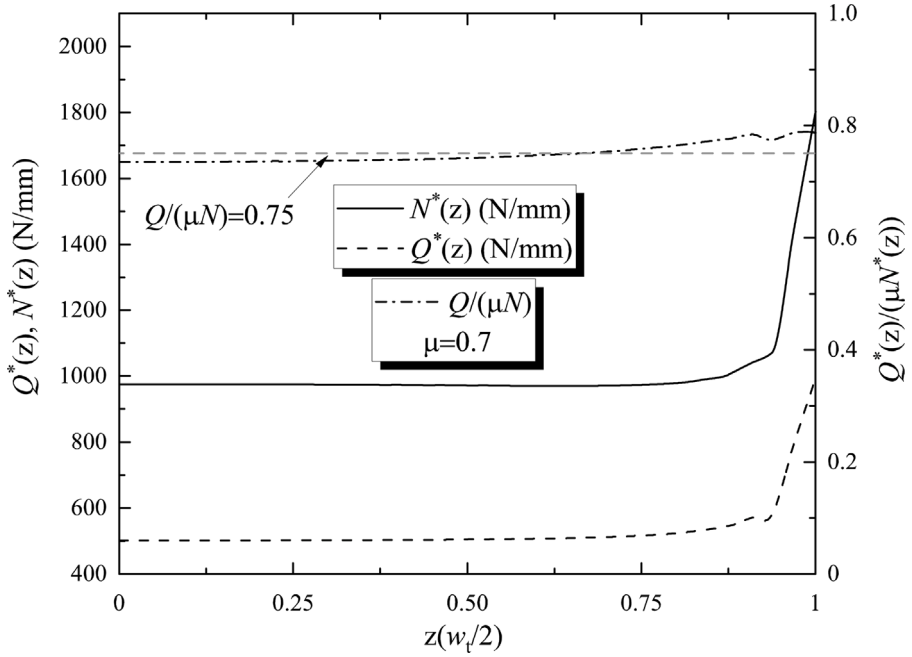

Fig. 18. Variation of $N^*(z)$ and $Q^*(z)$ and fretting load ratio $Q^*(z)/(\mu N^*(z))$ along test specimen's width in the case of $w_p = w_t$ at the contact surface, but test specimen having a variable width.

Although this is a very simple fatigue parameter, it is observed that in many situations fretting cracks nucleates nearly perpendicular to this stress [28], and thus this parameter could be an indicator of the most damaged zone.

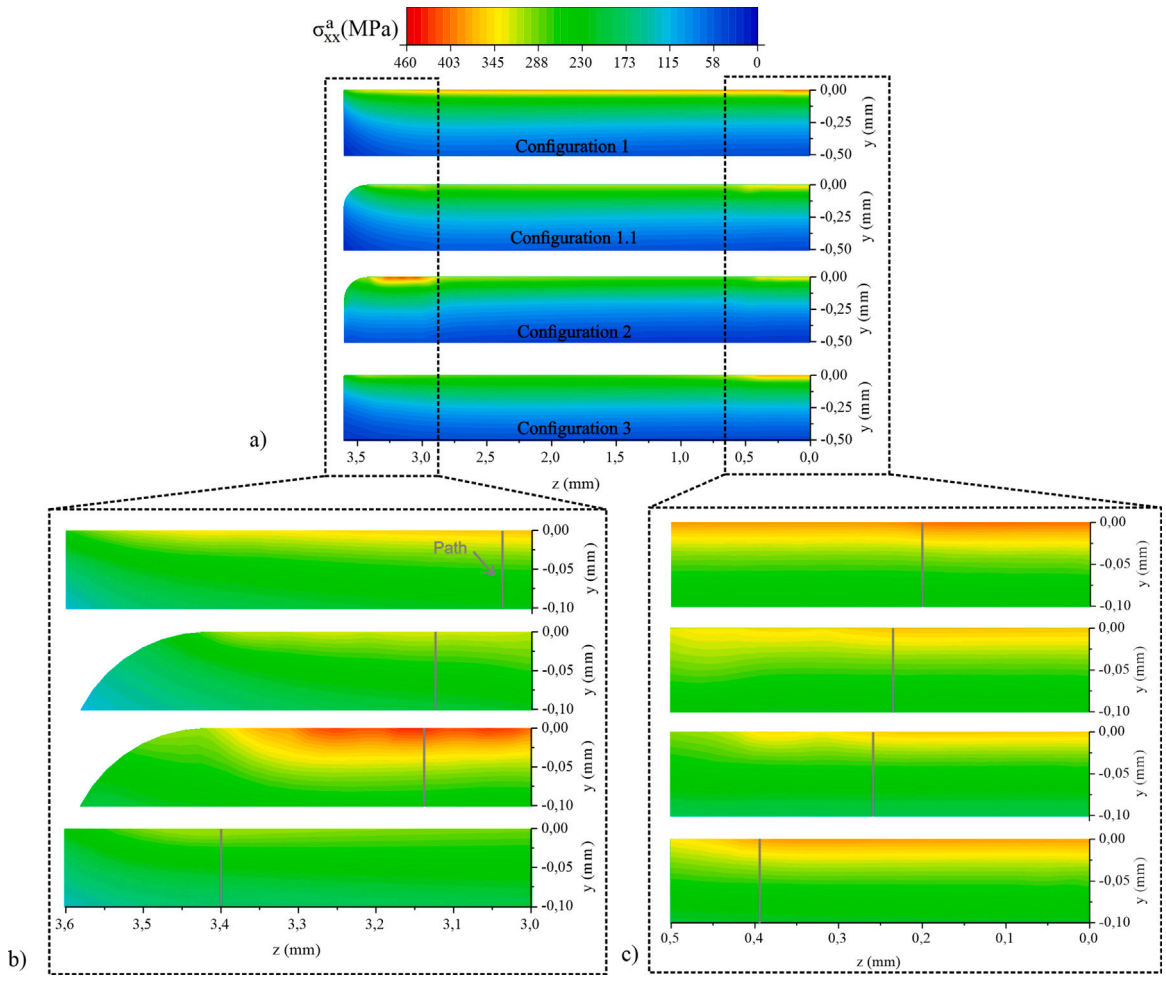

Fig. 19. (a) Contour plot for σ^{a}_{xx} along the yz plane, (b) Zoom for the contour plot at near border area, (c) Zoom for the contour plot at near middle-width area.

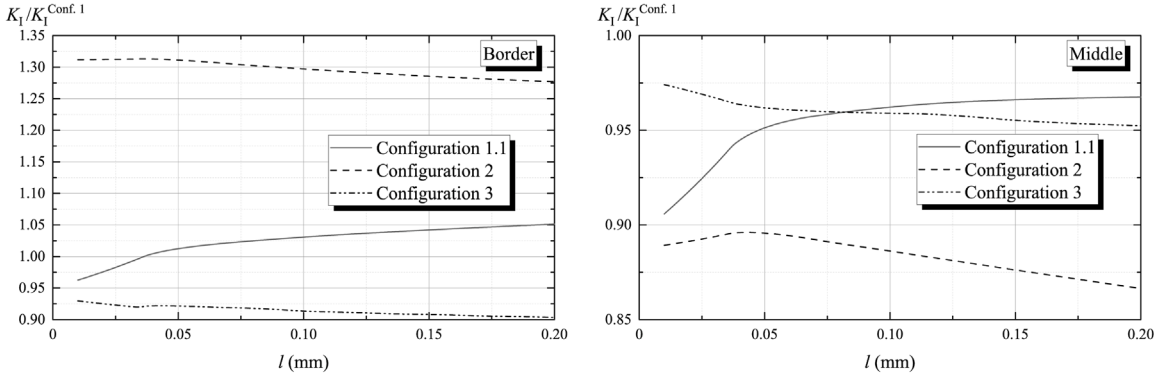

Fig. 20. (a) Normalised mode I SIF, K_I, for crack emanating from surface points located at near border area, (b) Normalised mode I SIF, K_I, for crack emanating from surface points located at the near middle-width area.

The results are shown in Fig. 19 for all the configurations and are depicted along the whole specimen thickness and up to a depth of 0.5 mm. Besides, a detailed view of the areas of interest are shown; a zoom for the first 100 μm (Fig. 19b and c). Analysing Fig. 19a, it can be observed that in a general way the behaviour obtained for all configurations is different on the surface, but the further we go from the surface, the more similar they are.

For a deeper analysis, specifically for the crack initiation assessment, the results should be analysed in a more detailed zone: in the order of the material grain size, which for the case of a typical high strength aluminium alloy could be around 50 μm. Analysing Fig. 19c for the area close to the middle-width test specimen section, it is shown that there is no a notable variation between all the configurations. Although slightly larger stress values are observed for configurations 1 and 3, they are located between the contact surfaces and up to a depth of 25 μm. In fact, similar averaged stress amplitudes along the depth are observed at the middle width zone, which could indicate that although differences at the contact surface stresses are obtained, they do not affect to a great extent if stresses are averaged along the depth. Fig. 19b depicts a detailed view for the areas close to the test specimen border. In those zones it can be applied the same comment made previously with the middle-width areas. The exception is the

border zone of configuration 2 where higher stress values than the rest are observed, although only in the very near contact surface material; about 50 μm. This may indicate a clear zone prone to crack initiation. For deeper points the stress values are similar to those obtained with the other configurations.

As a first analysis for the early fatigue crack growth, the maximum value along a fretting cycle for the mode I stress intensity factor (SIF), K_I, is computed for surface perpendicular cracks and emanating from the contact trailing edge at the most damaged points: surface points for the paths represented by vertical lines in Fig. 19b and c. Then cracks are assumed to growth under the influence of the direct stress, σ_{xx}, acting along the paths. In this fracture mechanics analysis it is assumed that in a cycle the tangential load, Q, is fully reversed.

To obtain the K_I for surface fretting cracks, the weight function technique is used here, specifically, the weight function, $w(l,s)$, proposed by Bueckner and Sih for the case of a surface through crack in a semi-infinite plate [81], is considered. Additionally, and in order to be closer to actual fretting cracks, a SIF corrective factor, Φ, for accounting the semi-elliptical shape of fretting surface cracks is taken [82]. Therefore, the SIF factor is computed as:

$$K_I = \frac{\int_0^l \sigma(s)\, w(l,s)\, ds}{\Phi} \tag{1}$$

where l is the deepest crack length, $w(l,s)$ is:

$$w(l,s) = \sqrt{\frac{2}{\pi s}}\left(1 + m_1\left(\frac{s}{l}\right) + m_2\left(\frac{s}{l}\right)^2\right) \tag{2}$$

and the correction factor, Φ, is defined by the following complete elliptic integral of the second kind:

$$\Phi = \int_0^{\frac{\pi}{2}} \sqrt{\sin^2\phi + \left(\frac{l}{c}\right)^2 \cos^2\phi}\, d\phi \approx \sqrt{1 + 1.464\left(\frac{l}{c}\right)^{1.65}}, \text{ for } \frac{l}{c} < \frac{4}{3} \tag{3}$$

In Eq. (3)c is the surface crack length, and in Eq. (2) m_1 and m_2 are parameters that depend on the ratio between the crack length and test specimen height (crack aspect ratio), l/h_t, and are defined by:

$$m_1 = 0.6147 + 17.1844\left(\frac{l}{h_t}\right)^2 + 8.7822\left(\frac{l}{h_t}\right)^6 \tag{4}$$

$$m_2 = 0.2502 + 3.2889\left(\frac{l}{h_t}\right)^2 + 70.0444\left(\frac{l}{h_t}\right)^6 \tag{5}$$

It is well known that the crack aspect ratio, l/h_t, varies during the fatigue crack growth process, for this reason the evolution shown in Figure 6 of [32] is here considered.

Results for the computed K_I distributions are shown in Fig. 20. In that figure results are normalised by the K_I values obtained with the configuration 1, that is here considered as the reference case.

Regarding the mode I SIF, a behaviour similar to that observed with the results of Fig. 19 is obtained. The evolution of K_I for configurations 1.1 and 3 is roughly similar to the one considered as reference case, independently of the zone. In regard to configuration 2, Fig. 20 shows that at the border zone is clearly the most unfavourable, with an increase of 30% in the SIF in mode I if compared with configuration 1. This means that if a typical value of 3 for the exponent of the Paris law was used, the crack growth rate would be 2.2 times higher in configuration 2 than in configuration 1, clearly affecting the fatigue crack growth in that zone. But an important fact to note here is that despite the border zone configuration 2 clearly shows the highest K_I values, at the middle-width zone it produces the lowest, indicating that likely the average fatigue crack growth rate along the width could be not so different to that in configurations 1.1 and 3, and thus all configurations could have a not significantly different fatigue crack growth behaviour.

4. Conclusions

According to the previous results the conclusions can be divided in two sections: conclusions obtained analysing only the contact surfaces and those obtained analysing the stress and SIFs below the contact surface.

In terms of contact stress distributions two specimen sections have been analysed, the one containing the middle-width section ($z = 0$) and the one at the free face of the specimen. The contact stresses obtained with the 3D model at the middle width section are compared with those obtained using an analytical 2D plane strain conditions, producing results very similar in both cases. Therefore, a bi-dimensional approach could be valid for this specific section. However, the results obtained at the free surface do not agree with those obtained using an analytical 2D approach, nor plane strain conditions neither plane stress. If the whole contact surface is observed in terms of normal pressure, the distributions remains in a reasonable variation for configurations 1 and 1.1. However, configurations 2 and 3 shows a very important variation between the middle-width section and the free surface, being the pressure of the free edge more than four times the one of the middle section for configuration 2. Therefore, from the point of view of contact stress distributions it is not clear that 2D models could represent the real behaviour of full 3D specimens, especially if crack nucleation and propagation is produced near or at the free surface.

From the point of view of axial stress below the contact zones. The main conclusion that can be drawn is that, although different contact stress distributions are observed at the contact surfaces, the axial stress tend to homogenised rapidly just below the contact surface. Nevertheless, this is not the case for configuration 2, where a clear zone more stresses is observed close to the specimen edge. The same comment can be addressed in terms of SIF in mode 1.

These results may lead to think that, from a more general point of view, and not as specific as the analysis just on the contact surface, the behaviour of configurations 1, 1.1 and 3 are very similar, and thus a 2D simplified model can approximately represent the whole 3D model, especially for the application of fretting fatigue models for lifetime prediction.

However, for all cases it is no yet sufficiently clear that the different types of contact pairs can produce substantially different results in terms of fatigue lifetime when compared to each other. Besides, in order to simplify this complex problem, several assumptions have been considered such as, the absence of a bulk stress and residual stresses and assuming a perfect surface finishing, factors that may modify the results obtained

To complete the analyses done here, some fretting tests and fatigue life simulations using the configurations shown here should be carried out in order to estimate the effect that this non uniform contact stress distribution along the test specimen width may have on the fatigue life

CRediT authorship contribution statement

J. Vázquez: Conception and design of study, Acquisition of data, Analysis and/or interpretation of data, Writing – original draft, Writing – review & editing. **D. Erena:** Conception and design of study, Acquisition of data, Analysis and/or interpretation of data, Writing – original draft, Writing – review & editing. **C. Navarro:** Conception and design of study, Analysis and/or interpretation of data, Writing – review & editing. **J. Domínguez:** Conception and design of study, Analysis and/or interpretation of data, Writing – review & editing.

Declaration of competing interest

The authors declare that they have no known competing financial interests or personal relationships that could have appeared to influence the work reported in this paper.

Acknowledgement

All authors approved the version of the manuscript to be published.

References

[1] D.A. Hills, D. Nowell, Mechanics of Fretting Fatigue, Kluber Academic Publishers, Dordrech/Boston/London, ISBN: 0-7923-2866-3, 1994.
[2] J.M. Dobromirski, Variables of fretting process: are there 50 of them? in: M.H. Attia, R.B. Waterhouse (Eds.), Standardization of Fretting Fatigue Test Methods and Equipment, in: ASTM STP 1159, Philadelphia, USA, 1992, pp. 60–66.
[3] R.B. Waterhouse, Fretting Fatigue, Applied Science Publisher, London, ISBN: 0-8529-8940-7, 1981.
[4] J. Vázquez, C. Navarro, J. Domínguez, Experimental results in fretting fatigue with shot and laser peened Al 7075-t651 specimens, Int. J. Fat. 40 (2012) 143–153, http://dx.doi.org/10.1016/j.ijfatigue.2011.12.014.
[5] R.B. Waterhouse, A.J. Trowsdale, Residual stress and surface roughness in fretting fatigue, J. Phys. D: Appl. Phys. 37 (1992) A236–A239, http://dx.doi.org/10.1088/0022-3727/25/1A/036.
[6] S. Mall, H.K. Kim, W.J. Porter, J.F. Ownby, A.G. Traylor, High temperature fretting fatigue behavior of IN100, Int. J. Fat. 32 (2010) 1289–1298, http://dx.doi.org/10.1016/j.ijfatigue.2010.01.012.
[7] J. Vázquez, C. Navarro, J. Domínguez, Analysis of the effect of a textured surface on fretting fatigue, Wear 305 (2013) 23–35, http://dx.doi.org/10.1016/j.wear.2013.05.003.
[8] ASTM E2789, Standard Guide for Fretting Fatigue Testing, ASTM International, 2015.
[9] D. Nowell, D.A. Hills, Mechanics of fretting fatigue tests, Int. J. Mech. Sci. 29 (1987) 355–365, http://dx.doi.org/10.1016/0020-7403(87)90117-2.
[10] R. Bramhall, Studies in Fretting Fatigue D.Phil. Thesis, University of Oxford, 1973.
[11] D.A. Hills, D. Nowell, J.J. O'Connor, On the mechanics of fretting fatigue, Wear 125 (1988) 129–156, http://dx.doi.org/10.1016/0043-1648(88)90198-6.
[12] M.P. Szolwinski, T.N. Farris, Observation, analysis and prediction of fretting fatigue in 2024-T351 aluminum alloy, Wear 221 (1998) 24–36, http://dx.doi.org/10.1016/S0043-1648(98)00264-6.
[13] A. Mugadu, D.A. Hills, D. Nowell, Modifications to a fretting-fatigue testing apparatus based upon an analysis of contact stresses at complete and nearly complete contacts, Wear 252 (2002) 475–483, http://dx.doi.org/10.1016/S0043-1648(02)00007-8.
[14] Reza Hojjati-Talemi, Magd Abdel Wahab, Jan De Pauw, Patrick De Baets, Prediction of fretting fatigue crack initiation and propagation lifetime for cylindrical contact configuration, Tribol. Int. 76 (2014) 73–91, http://dx.doi.org/10.1016/j.triboint.2014.02.017.
[15] J.A. Araújo, L. Susmel, D. Taylor, J.C.T. Ferro, E.N. Mamiya, On the use of the theory of critical distances and the modified wöhler curve method to estimate fretting fatigue strength of cylindrical contacts, Int. J. Fat. 29 (2007) 95–107, http://dx.doi.org/10.1016/j.ijfatigue.2006.02.041.
[16] B.U. Wittkowsky, P.R. Birch, J. Domínguez, S. Suresh, Experimental investigation of fretting fatigue with spherical contact in 7075-T6 aluminum alloy, in: Current Technology and Practices, ASTM International, 2000, http://dx.doi.org/10.1520/STP1367-EB.
[17] B.U.Wittkowsky, P.R. Birch, J. Dominguez, S. Suresh, An apparatus for quantitative fretting testing, Fatigue Fract. Eng. Mater. Struct. 22 (1999) 307–320, http://dx.doi.org/10.1046/j.1460-2695.1999.00145.x.
[18] B. Alfredsson, A. Cadario, A study on fretting friction evolution and fretting fatigue crack initiation for a spherical contact, Int. J. Fat. 26 (2004) 1037–1052, http://dx.doi.org/10.1016/j.ijfatigue.2004.03.010.
[19] T.A. Venkatesh, B.P. Conner, S. Suresh, et al., An experimental investigation of fretting fatigue in Ti-6Al-4V: the role of contact conditions and microstructure, Metall. Mater. Trans. A 32 (2001) 1131–1146, http://dx.doi.org/10.1007/s11661-001-0124-8.
[20] A.L. Hutson, T. Nicholas, R. Goodman, Fretting fatigue of Ti–6Al–4V under flat-on-flat contact, Int. J. Fat. 21 (1999) 663–669, http://dx.doi.org/10.1016/S0142-1123(99)00027-4.
[21] J. Kwon, H. Jeung, I. Chung, D. Yoon, D. Park, A study on fretting fatigue characteristics of inconel 690 at high temperature, Tribol. Int. 44 (2011) 148–1483, http://dx.doi.org/10.1016/j.triboint.2010.11.006.
[22] Y. Mutoh, K. Tanaka, Fretting fatigue in several steels and a cast iron, Wear 125 (1988) 175–191, http://dx.doi.org/10.1016/0043-1648(88)90201-3.
[23] Y. Mutoh, J.Q. Xu, K. Kondoh, Observations and analysis of fretting fatigue crack initiation and propagation, in: Y. Mutoh, D.W. Hoeppner, S.E. Kinyon (Eds.), Fretting Fatigue: Advances in Basic Understanding and Applications, in: ASTM STP 1425, 2003, pp. 61–75.
[24] Y. Mutoh, Q.X. Jin, Fracture mechanics approach to fretting fatigue and problems to be solved, Tribol. Int. 36 (2003) 99–107, http://dx.doi.org/10.1016/S0301-679X(02)00136-6.
[25] K. Nakazawa, N. Maruyama, T. Hanawa, Effect of contact pressure on fretting fatigue of austenitic stainless steel, Tribol. Int. 36 (2003) 79–85, http://dx.doi.org/10.1016/S0301-679X(02)00135-4.
[26] K.K. Liu, M.R. Hill, The effects of laser peening and shot peening on fretting fatigue in Ti–6Al–4V coupons, Tribol. Int. 42 (2009) 1250–1262, http://dx.doi.org/10.1016/j.triboint.2009.04.005.
[27] R.M.N. Fleury, R.J.H. Paynter, D. Nowell, The influence of contacting Ni-based single-crystal superalloys on fretting fatigue of Ni-based polycrystalline superalloys at high temperature, Tribol. Int. 76 (2014) 63–72, http://dx.doi.org/10.1016/j.triboint.2014.01.011.
[28] J. Vázquez, C. Navarro, J. Domínguez, Analysis of fretting fatigue initial crack path in Al7075-t651 using cylindrical contact, Tribol. Int. 208 (2017) 87–94, http://dx.doi.org/10.1016/j.triboint.2016.09.023.
[29] C. Navarro, J. Vázquez, J. Domínguez, Nucleation and early crack path in fretting fatigue, Int. J. Fatigue 100 (2017) 602–610, http://dx.doi.org/10.1016/j.ijfatigue.2016.12.028.
[30] J. Vázquez, A. Carpinteri, L. Bohórquez, S. Vantadori, Fretting fatigue investigation on Al 7075-T651 alloy: Experimental, analytical and numerical analysis, Tribol. Int. 135 (2019) 478–487, http://dx.doi.org/10.1016/j.triboint.2019.03.028.
[31] J. Vázquez, C. Navarro, J. Domínguez, A new method for obtaining the stress field in plane contacts, Int. J. Solids Struct. 49 (2012) 3659–3665.
[32] J. Vázquez, C. Navarro, J. Domí nguez, Two dimensional versus three dimensional modelling in fretting fatigue life prediction, J. Strain. Anal. Eng. Des. 51 (2016) 109–117, http://dx.doi.org/10.1177/0309324715611510.
[33] Y. Mutoh, K. Tanaka, M. Kondoh, Fretting fatigue in JIS S45C STEEL under 2-step block loading, JSME Int. J. 30 (1987) 386–393, http://dx.doi.org/10.1299/jsme1987.30.386.
[34] N. Noraphaiphipaksa, A. Manonukul, C. Kanchanomai, Fretting fatigue with cylindrical-on-flat contact: crack nucleation, crack path and fatigue life, Materials 10 (2017) 1–21, http://dx.doi.org/10.3390/ma10020155.
[35] N. Noraphaiphipaksa, C. Kanchanomai, Y. Mutoh, Numerical and experimental investigations on fretting fatigue: Relative slip, crack path, and fatigue life, Eng. Fract. Mech. (2013) 112–113, http://dx.doi.org/10.1016/j.engfracmech.2013.10.007, 58-71.
[36] D. Nowell, D. Dini, D.A. Hills, Recent developments in the understanding of fretting fatigue, Eng. Fract. Mech. 73 (2006) 207–222, http://dx.doi.org/10.1016/j.engfracmech.2005.01.013.
[37] R.M.N. Fleury, R.J.H. Paynter, D. Nowell, Estimation of the coefficient of friction in partial slip contacts between contacting nickel superalloys, Tribol.Int. 108 (2017) 156–163, http://dx.doi.org/10.1016/j.triboint.2016.09.039.
[38] M. Jayaprakash, Y. Mutoh, K. Asai, K. Ichikawa, S. Sukarai, Effect of contact pad rigidity on fretting fatigue behavior of NiCrMoV turbine steel, Int. J. Fat. 32 (2010) 1788–1794, http://dx.doi.org/10.1016/j.ijfatigue.2010.04.005.
[39] J.M. Wallace, R.W. Neu, Fretting fatigue crack nucleation in Ti–6Al–4V, fatigue, Fract. Eng. Mater. Struct. 25 (2003) 199–214, http://dx.doi.org/10.1046/j.1460-2695.2003.00553.x.
[40] Y. Mutoh, M. Jayaprakash, Tangential stress range–compressive stress range diagram for fretting fatigue design curve, Tribol. Int. 44 (2011) 1394–1399, http://dx.doi.org/10.1016/j.triboint.2010.10.013.
[41] C.-H. Goh, J.M. Wallace, R.W. Neu, D.L. McDowell, Polycrystal plasticity simulations of fretting fatigue, Int. J. Fat. 23 (2001) 423–435, http://dx.doi.org/10.1016/S0142-1123(01)00150-5.
[42] M. Jayaprakash, S. Anchalee, Y. Otsuka, Y. Mutoh, TSR–CSR diagram for 304 stainless steel, Int. J. Fat. 54 (2013) 99–105, http://dx.doi.org/10.1016/j.ijfatigue.2013.04.003.
[43] A.L. Hutson, T. Nicholas, S.E. Olson, N.E. Ashbaugh, Effect of sample thickness on local contact behavior in a flat-on-flat fretting fatigue apparatus, Int. J. Fat. 23 (2001) 445–453, http://dx.doi.org/10.1016/S0142-1123(01)00142-6.
[44] S.A. Namjoshi, V.K. Jain, S. Mall, Ffects of shot-peening on fretting-fatigue behavior of Ti-6Al-4V, J. Eng. Mater. Technol. 124 (2002) 222–228, http://dx.doi.org/10.1115/1.1448323.
[45] A.L Hutson, C. Neslen, T. Nicholas, Characterization of fretting fatigue crack initiation processes in CR Ti–6Al–4V, Tribol. Int. 36 (2003) 133–143, http://dx.doi.org/10.1016/S0301-679X(02)00138-X.
[46] S. Shkarayev, S. Mall, Computational modelling of shot-peening effects on crack propagation under fretting fatigue, J. Strain. Analy. 38 (2003) 495–506, http://dx.doi.org/10.1243/030932403770735863.
[47] T. Nicholas, A. Hutson, R. John, S. Olson, A fracture mechanics methodology assessment for fretting fatigue, Int. J. Fat. 25 (2003) 1069–1077, http://dx.doi.org/10.1016/S0142-1123(03)00115-4.
[48] H. Lee, O. Jin, S. Mall, Fretting fatigue behaviour of shot-peened Ti-6Al-4V at room and elevated temperatures, Fatigue Fract. Eng. Mater. Struct. 26 (2003) 767–778, http://dx.doi.org/10.1046/j.1460-2695.2003.00677.x.
[49] A. Hutson, T. Nicholas, R. John, Fretting fatigue crack analysis in Ti–6Al–4V, Int. J. Fat. 27 (2005) 1582–1589, http://dx.doi.org/10.1016/j.ijfatigue.2005.07.008.
[50] C.D. Lykins, S. Mall, V.K. Jain, Combined experimental–numerical investigation of fretting fatigue crack initiation, Int. J. Fat. 23 (2001) 703–711, http://dx.doi.org/10.1016/S0142-1123(01)00029-9.
[51] V. Sabelkin, S. Mall, Relative slip on contact surface under partial slip fretting fatigue condition, Strain 42 (2006) 11–20, http://dx.doi.org/10.1111/j.1475-1305.2006.00248.x.

[52] S. Mall, V.K. Jain, H.A. Fadag, Effects of shot-peening on fretting fatigue crack growth behavior in Ti-6Al-4V, Strain 47 (2011) 305–318, http://dx.doi.org/10.1111/j.1475-1305.2008.00591.x.
[53] S.A. Namjoshi, S. Mall, V.K. Jain, O. Jin, Fretting fatigue crack initiation mechanism in Ti–6Al–4V, Fatigue Fract. Eng. Mater. Struct. 25 (2002) 955–964, http://dx.doi.org/10.1046/j.1460-2695.2002.00549.x.
[54] O. Jin, S. Mall, Effects of independent pad displacement on fretting fatigue behavior of Ti–6Al–4V, Wear 253 (2002) 585–596, http://dx.doi.org/10.1016/S0043-1648(02)00061-3.
[55] C.D. Lykins, S. Mall, V. Jain, A shear stress-based parameter for fretting fatigue crack initiation, Fatigue Fract. Eng. Mater. Struct. 24 (2001) 461–473, http://dx.doi.org/10.1046/j.1460-2695.2001.00412.x.
[56] O. Jin, S. Mall, Effects of slip on fretting behavior: experiments and analyses, Wear 256 (2004) 671–684, http://dx.doi.org/10.1016/S0043-1648(03)00510-6.
[57] H. Murthy, G. Mseis, T.N. Farris, Life estimation of Ti–6Al–4V specimens subjected to fretting fatigue and effect of surface treatments, Tribol. Int. 42 (2009) 1304–1315, http://dx.doi.org/10.1016/j.triboint.2009.04.013.
[58] R. Magaziner, O. Jin, S. Mall, Slip regime explanation of observed size effects in fretting, Wear 257 (2004) 190–197, http://dx.doi.org/10.1016/j.wear.2003.12.005.
[59] S. Srinivasan, D.B. Garcia, M.C. Gean, H. Murthy, T.N. Farris, Fretting fatigue of laser shock peened Ti–6Al–4V, Tribol. Int. 42 (2009) 1324–1329, http://dx.doi.org/10.1016/j.triboint.2009.04.014.
[60] E. Giner, M. Sabsabi, J.J. Ródenas, F.J. Fuenmayor, Direction of crack propagation in a complete contact fretting-fatigue problem, Int. J. Fat. 58 (2014) 172–180, http://dx.doi.org/10.1016/j.ijfatigue.2013.03.001.
[61] J.J. Madge, S.B. Leen, I.R. McColl, P.H. Shipway, Contact-evolution based prediction of fretting fatigue life: Effect of slip amplitude, Wear 262 (2007) 159–1170, http://dx.doi.org/10.1016/j.wear.2006.11.004.
[62] A.A. Walvekar, B.D. Leonard, F. Sadeghi, B. Jalalahmadi, N. Bolander, An experimental study and fatigue damage model for fretting fatigue, Tribol. Int. 79 (2014) 183–196, http://dx.doi.org/10.1016/j.triboint.2014.06.006.
[63] N. Noraphaiphipaksa, A. Manonukul, C. Kanchanomai, Fretting fatigue with cylindrical-on-flat contact: Crack nucleation, crack path and fatigue life, Materials 10 (2017) 1–21, http://dx.doi.org/10.3390/ma10020155.
[64] F. Abbasi, G.H. Majzoobi, Effect of out-of-phase loading on fretting fatigue response of Al7075-T6 under cyclic normal loading using a new testing apparatus, Eng. Fract. Mech. 188 (2018) 93–111, http://dx.doi.org/10.1016/j.engfracmech.2017.08.010.
[65] J. Kwon, D. Park, S. Woo, D. Yoon, I. Chung, A study on fretting fatigue life for the inconel alloy 600 at high temperature, Nucl. Eng. Des. 240 (2010) 2521–2527, http://dx.doi.org/10.1016/j.nucengdes.2010.05.013.
[66] F. Abbasi, G.H. Majzoobi, An investigation into the effect of elevated temperatures on fretting fatigue response under cyclic normal contact loading, Theor. Appl. Fract. Mech. 93 (2018) 144–154, http://dx.doi.org/10.1016/j.tafmec.2017.07.018.
[67] G.H. Majzoobi, F. Abbasi, An investigation into the effect of normal load frequency on fretting fatigue behavior of Al7075-T6, Tribol. Trans. 61 (2018) 547–559, http://dx.doi.org/10.1080/10402004.2017.1371366.
[68] G.H. Majzoobi, A.R. Ahmadkhani, The effects of multiple re-shot peening on fretting fatigue behavior of al7075-T6, Surf. Coat. Technol. 205 (2010) 102–109, http://dx.doi.org/10.1016/j.surfcoat.2010.06.014.
[69] J. Takeda, M. Niinomi, T. Akahori, Gunawarman, Fretting fatigue characteristics with relating contact pressure and surface roughness of highly workable titanium alloy, Ti-4.5Al-3V-2Mo-2Fe, materials transactions, JIM 45 (2004) 1586–1593, http://dx.doi.org/10.2320/matertrans.45.1586.
[70] D. Nowell, An Analysis of Fretting Fatigue D.Phil. Thesis, University of Oxford, 1988.
[71] N.K. Ramakrishna Naidu, S.G. Sundara Raman, Effect of shot blasting on plain fatigue and fretting fatigue behaviour of Al–Mg–Si alloy AA6061, Int. J. Fat. 27 (2005) 323–331, http://dx.doi.org/10.1016/j.ijfatigue.2004.07.007.
[72] J.A. Araújo, D. Nowell, Mixed high low fretting fatigue of Ti6Al4V: Tests and modelling, Tribol. Int. 42 (2009) 1276–1285, http://dx.doi.org/10.1016/j.triboint.2009.04.024.
[73] N.K. Ramakrishna Naidu, S.G. Sundara Raman, Effect of contact pressure on fretting fatigue behaviour of Al–Mg–Si alloy AA6061, Int. J. Fat. 27 (2005) 283–291, http://dx.doi.org/10.1016/j.ijfatigue.2004.07.001.
[74] L.S. Rossino, F.C. Castro, W.W. Bose Filho, J.A. Araújo, Issues on the mean stress effect in fretting fatigue of a 7050-T7451 Al alloy posed by new experimental data, Int.L J. Fat. 31 (2009) 2041–2048, http://dx.doi.org/10.1016/j.ijfatigue.2008.12.011.
[75] B. Rengaraj, S. Baba, M. OkazakiI, Role of tangential force coefficient on fretting fatigue life estimation of a single crystal Ni-base superalloy, Mech. Eng. J. 4 (2017) http://dx.doi.org/10.1299/mej.17-00187.
[76] V. Martín, J. Vázquez, C. Navarro, J. Domínguez, Fretting-fatigue analysis of shot-peened Al 7075-T651 test specimens, Metals (Basel) 9 (2019) 586.
[77] D. Nowell, D. Hills, R. Moobola, Length scale considerations in fretting fatigue Frett, in: Fatigue Curr. Technol. Pract, ASTM International, 2000, pp. 141–141–13, http://dx.doi.org/10.1520/STP14726S.
[78] D. Dini, D. Nowell, A.M. Korsunsky, Size and scale effects in fretting fatigue thresholds, Int. J. Fract. 135 (2005) L11–8, http://dx.doi.org/10.1007/s10704-005-4390-0.
[79] J. Vázquez, C. Navarro, J. Domínguez, On the estimation of fatigue life in notches differentiating the phases of crack initiation and propagation, Fatigue Fract. Eng. Mater. Struct. 33 (2010) 22–36, http://dx.doi.org/10.1111/j.1460-2695.2009.01411.x.
[80] J.R. Barber, Elasticity, in: Solid Mechanics and Its Applications, Springer, Dordrecht, 2010, http://dx.doi.org/10.1007/978-90-481-3809-8.
[81] G.C. Sih, editor, Methods of Analysis and Solutions of Crack Problems, Springer Netherlands, Dordrecht, 1973, http://dx.doi.org/10.1007/978-94-017-2260-5.
[82] G.R. Irwin, Crack-extension force for a part-through crack in a plate, J. Appl. Mech. 29 (1962) 4–651, http://dx.doi.org/10.1115/1.3640649.